Article

Developmental Cell

Characterization of the structure and control of the blood-nerve barrier identifies avenues for therapeutic delivery

Graphical abstract

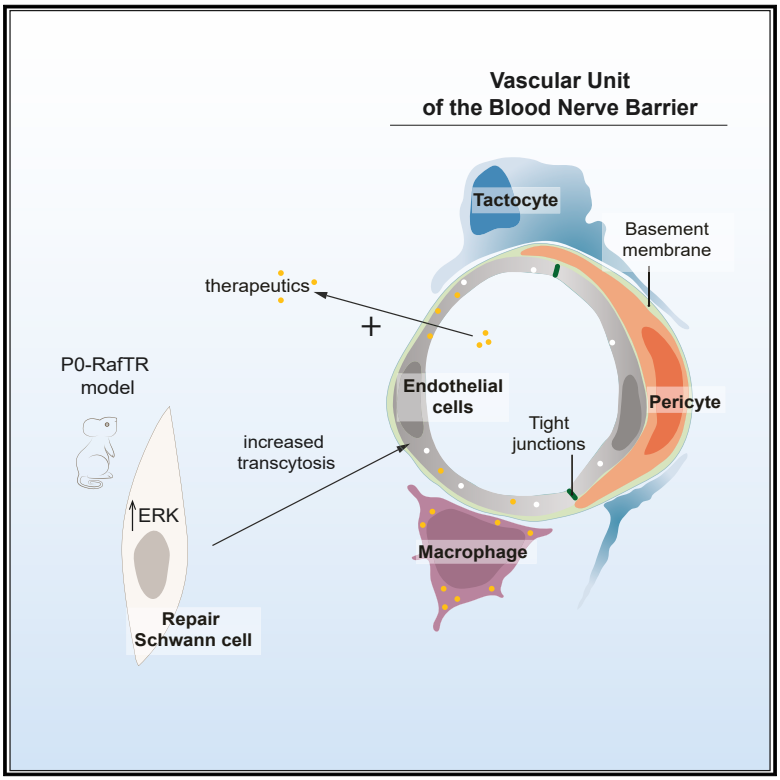

Authors

Liza Malong, Ilaria Napoli, Giulia Casal, ..., Adrienne Flanagan, Hien T. Zhao, Alison C. Lloyd

Correspondence

alison.lloyd@ucl.ac.uk

In brief

Malong et al. characterize the conserved multicellular structures and processes that define the mammalian blood-nerve barrier (BNB). Macrophages enforce the BNB during homeostasis, whereas, following injury, Schwann cells transiently "open" the barrier by increasing transcytosis rates across blood vessels, permitting increased delivery of therapeutics to peripheral nerves.

Highlights

- Definition of the vascular unit of the mammalian blood-nerve barrier
- Macrophages enforce barrier function during homeostasis
- Schwann cells open the barrier following injury by increasing transcytosis
- Increased transcytosis improves the delivery of therapeutics to nerves

Malong et al., 2023, Developmental Cell *58*, 1–18
February 6, 2023
https://doi.org/10.1016/j.devcel.2023.01.002

CellPress

Developmental Cell

CellPress
OPEN ACCESS

Article

Characterization of the structure and control of the blood-nerve barrier identifies avenues for therapeutic delivery

Liza Malong,[1,3] Ilaria Napoli,[1,3] Giulia Casal,[1,3] Ian J. White,[1] Salome Stierli,[1] Andrew Vaughan,[1] Anne-Laure Cattin,[1] Jemima J. Burden,[1] Keng I. Hng,[1] Alessandro Bossio,[1] Adrienne Flanagan,[1] Hien T. Zhao,[2] and Alison C. Lloyd[1,4,*]

[1]UCL Laboratory for Molecular Cell Biology and UCL Cancer Institute, University College London, Gower Street, London, WC1E 6BT, UK
[2]IONIS, 2855 Gazelle Court, Carlsbad, CA 92010, USA
[3]These authors contributed equally
[4]Lead contact
*Correspondence: alison.lloyd@ucl.ac.uk
https://doi.org/10.1016/j.devcel.2023.01.002

SUMMARY

The blood barriers of the nervous system protect neural environments but can hinder therapeutic accessibility. The blood-brain barrier (BBB) is well characterized, consisting of endothelial cells with specialized tight junctions and low levels of transcytosis, properties conferred by contacting pericytes and astrocytes. In contrast, the blood-nerve barrier (BNB) of the peripheral nervous system is poorly defined. Here, we characterize the structure of the mammalian BNB, identify the processes that confer barrier function, and demonstrate how the barrier can be opened in response to injury. The homeostatic BNB is leakier than the BBB, which we show is due to higher levels of transcytosis. However, the barrier is reinforced by macrophages that specifically engulf leaked materials, identifying a role for resident macrophages as an important component of the BNB. Finally, we demonstrate the exploitation of these processes to effectively deliver RNA-targeting therapeutics to peripheral nerves, indicating new treatment approaches for nervous system pathologies.

INTRODUCTION

Blood vessels permeate all tissues of the body allowing the exchange of substances required for normal tissue function. The degree of blood vessel permeability differs between tissues with the specialization of endothelial cells (ECs) responsible for tissue differences,[1,2] for example, fenestrated liver ECs are responsible for the increased permeability of the vasculature important for liver function.[3] In contrast, the CNS requires a highly protected environment that is provided by the most selective blood vessels of the body that form the blood-brain barrier (BBB).[4–6] The BBB is considered essential for the health of the CNS but has proven a problematic barrier to the delivery of therapeutics.[7–9]

The barrier function of the BBB is the result of ECs with low rates of transcytosis and strengthened tight junctions that inhibit transcellular and paracellular transport, respectively.[10–15] The exchange of substances to maintain CNS function is mediated by influx and efflux transporters and receptor-mediated transcytosis across the ECs.[14,16] This specialization of CNS ECs is not cell-intrinsic but is conferred by signals from other cell types that compose the vascular unit of the BBB.[17–22] Pericytes and astrocytes provide near-complete coverage of CNS vessels,[23,24] and their interactions with ECs provide the signals responsible for the development and the maintenance of their barrier properties.[24–27] In contrast, the blood-nerve barrier (BNB), which protects peripheral nerves, is poorly defined. What is known is that the BNB matures postnatally[28–30] and that the structure of the vascular unit must be different—as astrocytes do not exist in the peripheral nervous system (PNS) and that the barrier is less tight than that of the CNS.[31–33] Understanding the structure and regulation of the BNB has important therapeutic implications. In addition to the BNB hindering the delivery of therapeutics to the PNS,[34,35] the loss of BNB integrity is associated with peripheral neuropathies.[36] Moreover, differential properties of the BBB and the BNB are thought to be responsible for chemotherapy-induced neuropathies—a major limiting factor in these treatments.[37]

In previous work, using a mouse model that mimics the regenerative response of Schwann cells (SCs) following nerve injury, we showed that signals from repair SCs were sufficient to open the BNB,[38] providing a model system to understand the regulation of barrier function. Here, we define the cellular composition of the vascular unit that comprises the mammalian BNB, determine the processes underlying barrier function, and demonstrate how this can be modified to open the barrier in response to injury signals. In addition, we identify a role for macrophages in BNB function, acting to "hoover-up" leakage across

Please cite this article in press as: Malong et al., Characterization of the structure and control of the blood-nerve barrier identifies avenues for therapeutic delivery, Developmental Cell (2023), https://doi.org/10.1016/j.devcel.2023.01.002

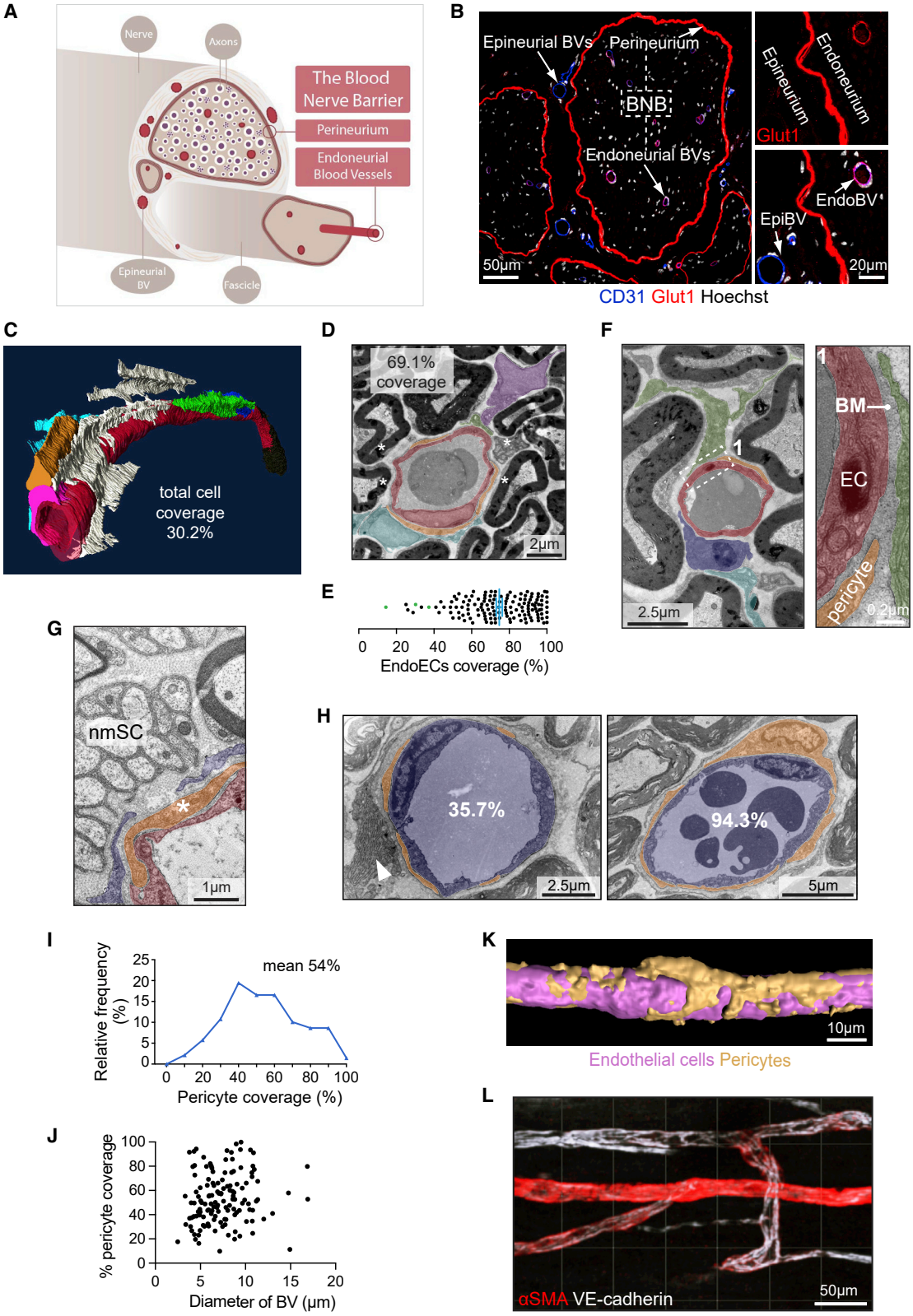

Figure 1. Definition of the vascular unit of the blood-nerve barrier

(A) Schematic illustrating the two components of the BNB.

(B) Representative confocal images of transverse sections of mouse sciatic nerve showing Glut1 expression (red).

(legend continued on next page)

Please cite this article in press as: Malong et al., Characterization of the structure and control of the blood-nerve barrier identifies avenues for therapeutic delivery, Developmental Cell (2023), https://doi.org/10.1016/j.devcel.2023.01.002

the barrier. Finally, we demonstrate how we can increase the delivery of therapeutics to the PNS providing a paradigm for delivering drugs to the nervous system.

RESULTS

Definition of the vascular unit of the BNB

In peripheral nerves, the protection of the endoneurium by the BNB exists at two levels: (1) endoneurial blood vessels (EndoBVs) and (2) the perineurium (Figures 1A and 1B). The epineurium is highly vascularized,[39] but these blood vessels do not have barrier function and thereby provided a useful comparative control. The vast majority of EndoBVs are capillaries or small arterioles, judged by their size (87% <10 μm in diameter) (Figure S1A),[40] consistent with previous studies.[39,41] In contrast, epineurial blood vessels (EpiBVs) are more heterogeneous with many larger vessels, indicative of venules and arterioles (Figure S1A). Consistent with their barrier function, both EndoBVs and the perineurium of mouse sciatic nerves express the barrier-associated glucose transporter 1, Glut1,[42] whereas EpiBVs do not (Figure 1B). Additionally, barrier properties can be visualized with intravenous injection tracers, such as Evans blue, which stay restricted at the two levels of the barrier (Figure S1B).

In the CNS, blood vessels with barrier function are completely covered by other cell types, with a high degree of pericyte coverage with the remaining surface covered by the endfeet of astrocytes, with neuronal contacts to the surrounding cells.[23,25,43] Together, this structure is defined as the vascular unit that comprises the BBB.[40,43] To determine the cellular coverage of endoneurial ECs (EndoECs), we initially performed 3D electron microscopy (EM) of mouse sciatic nerves to detect cellular contacts along individual vessels. In contrast to the CNS, we found incomplete cellular coverage of PNS EndoECs with variable coverage between vessels (Figures 1C, S1C and S1D; Video S1). To quantify a greater number of EndoBVs, we analyzed high-resolution 2D EM images (Figure 1D, quantified in 1E) and found a mean coverage of 75.6% demonstrating that complete cellular coverage of EndoECs is not required for the BNB.

Analysis of the EM images found that cells with different morphologies were closely associated with the EndoBVs (Figures 1D, 1F, and S1E). In the CNS, pericytes are important for barrier function[23–25,27] and can be identified by their residency within the basement membrane (BM) and expression of specific markers. In previous work, we showed that pericytes within the endoneurium have a common signature, in that they all express NG2, PDGFRβ, and α-SMA.[44] In addition, we found that all endoneurial pericytes express the pericyte marker CD146/MCAM[22] (Figure S1F). Analysis of EM images could identify pericytes within the BM (Figures 1H and S1E), whereas other cell types interacted with the EndoBVs in a looser fashion, contacting the outer layer of the BM. The identity of the pericytes was confirmed by correlative light and EM (CLEM) using α-SMA expression as a marker (Figures S1F and S1G). Quantification of pericyte coverage from 2D-EM images (Figure 1H) found coverage varied between 10% and 100%, with a mean of 54% (Figure 1I), with no correlation to the size of individual BVs (Figure 1J). To complement the EM quantification, we quantified pericyte coverage from surface-rendered 3D confocal images of EndoBVs (Figures 1K and S1I; Video S2). Similarly, we found variability in coverage, with a lower mean of 33.86%, consistent with the lower sensitivity of this technique. The variability of pericyte coverage between BVs was further confirmed by 3D/PACT immunostaining and immunofluorescence images of sciatic nerve transverse sections (Figures 1L and S1F). Together, these results demonstrated that differing levels of pericyte coverage are sufficient for barrier function, as, despite variability in EC coverage, all EndoBVs exhibit barrier function.

Tactocytes and macrophages contribute to the vascular unit of the BNB

Our EM analysis showed cells with different morphologies were making looser contacts with EndoBVs indicating other cell types may play a similar role to astrocytes within the CNS. To identify these cells, we used our immunostaining toolbox that enables the identification of all cell types within the endoneurium,[44] together with EM analysis for high-resolution characterization of interacting cell types. Firstly, we analyzed SCs, which account for ~70% of cells in the endoneurium. However, although many were observed in close proximity to vessels, we failed to detect any direct interactions (Figures 1D–1G, 2A, and S1D). In contrast, we found that two other cell types, tactocytes and macrophages, were associated with all EndoBVs.

Tactocytes are poorly characterized fibroblast-like cells present within the endoneurium, described variously as fibroblasts,[45,46] telocytes,[47] pericyte-like cells/tactocytes,[44] or mesenchymal precursor cells.[48] We have previously shown they account for

(C) Serial block face (SBF)-SEM reconstruction of an EndoBV of mouse sciatic nerve shows ECs (red) with interacting cells individually colored. See Video S1.
(D) Representative TEM image of an EndoBV showing ECs (red), interacting cells within the BM (orange), and other interacting cells (individually colored). * indicate nearby SCs.
(E) Quantification of the coverage of EndoECs quantified from 2D-TEM (black dots) and 3D-SBF-SEM (green dots) images. Each dot represents a BV, mean ± SEM, n = 4 mice.
(F) Representative TEM images of cells contacting the BM of EndoECs (red). Pericytes (orange) were identified by their localization within the BM. Other cells (green, purple, and blue) were found more loosely associated via contact with the surface of the BM.
(G) Representative TEM image of a pericyte (orange) within the BM of an EC (red), with nearby SCs lacking direct contact with the BM.
(H) Representative TEM images of transverse sections of EndoBVs showing variable pericyte coverage. ECs and lumen (blue), pericytes (orange). The white arrowhead indicates another cell type making contact with the BM. Pericyte coverage is indicated.
(I) Graph shows the frequency distribution of pericyte coverage as seen in (H), mean ± SEM 54% ± 1.78%, n = 139 EndoBVs from 6 mice.
(J) Graph shows no correlation between pericyte coverage and size of vessel. Each dot represents an individual vessel, n = 6 mice.
(K) Representative 3D-surface reconstructed image of a longitudinal sciatic nerve section using antibodies to detect ECs (CD31, purple) and pericytes (αSMA, orange). See Video S2.
(L) 3D image of EndoBVs in a PACT-cleared sciatic nerve showing variable coverage of ECs (VE-cadherin, white) and pericytes (αSMA, red).
See also Figure S1.

Please cite this article in press as: Malong et al., Characterization of the structure and control of the blood-nerve barrier identifies avenues for therapeutic delivery, Developmental Cell (2023), https://doi.org/10.1016/j.devcel.2023.01.002

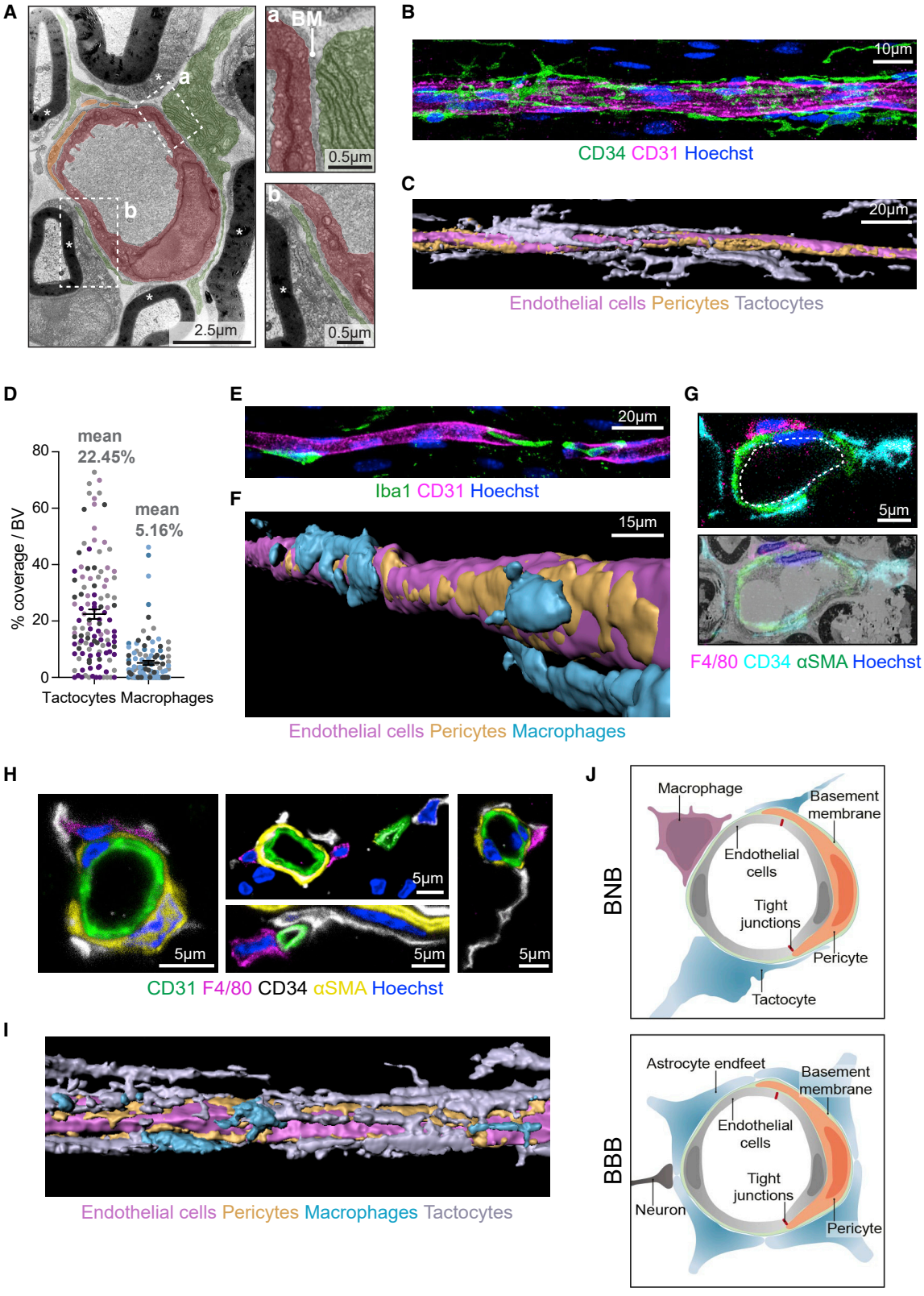

Figure 2. Tactocytes and macrophages contribute to the vascular unit of the BNB

(A) Representative TEM image of an EndoBV (EC, red) and surrounding cells. Pericytes (orange), tactocyte (green). Zooms show a tactocyte contacting the BM (upper panel), whereas an mSC (*), does not.

(legend continued on next page)

Please cite this article in press as: Malong et al., Characterization of the structure and control of the blood-nerve barrier identifies avenues for therapeutic delivery, Developmental Cell (2023), https://doi.org/10.1016/j.devcel.2023.01.002

~12.5% of endoneurial cells and express the pericyte markers NG2 and PDGFRβ and are p75+ but αSMA-negative.[44] They have a characteristic elongated and ER-rich morphology, and based on their contacts with other cell types within the endoneurium, we named them tactocytes.[44] In addition, we found they express the transmembrane glycoprotein CD34, a common marker of progenitor cells,[49] which is expressed along the elongated protrusions of these cells, permitting visualization of cell:cell contacts (Figures S2A–S2C). EM analysis of these ER-rich cells, the identity of which was confirmed by CLEM (Figure S2D), showed they make intimate contact with blood vessels (Figure 2A). Unlike pericytes, tactocytes interact with the exterior of the BM of the ECs (Figure 2A), making multiple contacts along the length of EndoBVs (Figure 2B) with other protrusions stretching into the endoneurium (Figures 2C and S2E; Video S3). Tactocyte contacts could be visualized at both regions of pericyte coverage and at pericyte-free regions (Figures 2A, 2C, S2A, and S2E) and appeared to be independent of the degree of pericyte coverage of individual blood vessels. Quantification of the degree of direct coverage confirmed the variability seen between and along the length of individual vessels with a mean coverage of 22.45% (Figure 2D).

The second cell type we identified associated with EndoBVs were macrophages. Resident macrophages make up around 4%–6% of the endoneurial cell population and all co-express F4/80 and Iba1.[44,50] A proportion of macrophages associated with EndoBVs (Figure S2F) and longitudinal sections showed them intimately associated along the length of vessels (Figures 2E–2F). Their identity in EM images was confirmed by CLEM (Figure S2G) and showed that similarly to tactocytes, they remain outside of the BM (Figure S1E) and make contacts both in regions of pericyte coverage and free of pericytes (Figures 2F and S2H; Video S4). Quantification of EC direct coverage by macrophages showed a lower level of coverage than tactocytes (mean 5.16%) with variability between the vessels (Figure 2D).

To further define the structure of the vascular unit, we used 2D and 3D immunostaining, together with CLEM to simultaneously visualize the interacting cell types (Figures 2G–2I and S2I–S2J; Video S5), and confirmed that no other cell types were making regular contact with the vessels. This allowed us to define the BNB vascular unit as ECs with closely interacting pericytes and more loosely associated tactocytes and macrophages (Figure 2J). Although there is some variability in the degree of coverage between regions of EndoBVs, a consistent multicellular structure could be observed. While there are similarities to the vascular unit comprising the BBB, the vascular unit of the BNB shows a different cellular composition and lower degree of cellular coverage while maintaining barrier function.

The vascular unit of the PNS is conserved across organisms and nerve types

We then addressed whether the PNS vascular unit is conserved in other mammalian species. In adult rats, Evans blue was restricted at the level of the perineurium and EndoECs (Figure S3A), and both expressed Glut1 (Figure S3B), consistent with previous studies.[51] Importantly, we identified a highly similar, multicellular structure, demonstrating the vascular unit is conserved in rats (Figures 3A–3B and S3C). Similar to mice, pericytes were embedded within the EC BM, whereas tactocytes and macrophages made contacts along the outside of the BM (Figure 3C). The only notable difference was that the cellular coverage of EndoECs was higher than in the mouse (94.6% versus 75.6%), mostly due to greater coverage by pericytes (Figures 3C–3E). This correlated with an increase in vessel size, perhaps reflecting a requirement for higher coverage in larger vessels (Figure S3D). Analysis of human peripheral nerves identified a similar vascular unit within the endoneurium (Figures 3F–3H and S3E–S3G). As in rodents, we observed that EndoECs were not always fully covered by other cell types (Figure S3G) and that pericyte coverage was variable, with mean coverage levels (74%) in between that of the mouse (54%) and rat (88%) (Figures 3E and S3E). Notably, using high-resolution 3D-EM analysis, we were able to observe extensive, reciprocal, peg-socket interactions between ECs and pericytes (Figure 3G insets), which are characteristic of pericyte/EC interactions in the CNS and have been proposed to mediate cell communication important for vascular homeostasis.[52]

Our initial analysis was of the mouse sciatic nerve, a large spinal nerve with a mixture of sensory and motor axons. To characterize other peripheral nerve types, we analyzed (1) facial cranial nerve-CN VII consisting of motor, sensory, and parasympathetic fibers and (2) the saphenous nerve, which consists solely of sensory axons. The exclusion of Evans blue showed they exhibited barrier function at the level of EndoECs and the perineurium. Moreover, the composition of the vascular unit was highly similar to the structure detected in the sciatic nerve (Figure S3H). Together, these results demonstrate the conservation of the

(B) Representative confocal image of a longitudinal section of an EndoBV in mouse sciatic nerve showing ECs (CD31, magenta) and tactocytes (CD34, green) making multiple contacts along the vessel.
(C) Representative 3D-surface reconstructed image of a longitudinal sciatic nerve section. EndoECs (CD31, purple), pericytes (αSMA, orange), and tactocytes (CD34, gray). See Video S3.
(D) Quantification of EndoEC coverage by tactocytes and macrophages from (C) and (F). Different shades represent individual mice. Each dot represents an EndoBV, n = 4 mice. Mean ± SEM.
(E and F) Representative confocal images of longitudinal sections of EndoBVs showing (E) ECs (CD31, green) and macrophages (Iba1, magenta) and (F) EndoECs (CD31, purple), pericytes (αSMA, orange), and macrophages (F4/80, blue). See Video S4.
(G) Representative CLEM image of an EndoBV labeled to detect tactocytes (CD34, cyan), macrophages (F4/80, red), and pericytes (αSMA, green).
(H) Representative confocal images of transverse sections of sciatic nerve labeled to detect ECs (CD31, green), pericytes (αSMA, yellow), tactocytes (CD34, white), and macrophages (F4/80, magenta).
(I) Representative 3D-surface reconstructed image of a longitudinal sciatic nerve section labeled to detect EndoECs (CD31, purple), pericytes (αSMA, orange), macrophages, (F4/80, blue), and tactocytes (CD34, gray). See Video S5.
(J) Schematics comparing the vascular unit of the BBB and BNB.
See also Figure S2.

Please cite this article in press as: Malong et al., Characterization of the structure and control of the blood-nerve barrier identifies avenues for therapeutic delivery, Developmental Cell (2023), https://doi.org/10.1016/j.devcel.2023.01.002

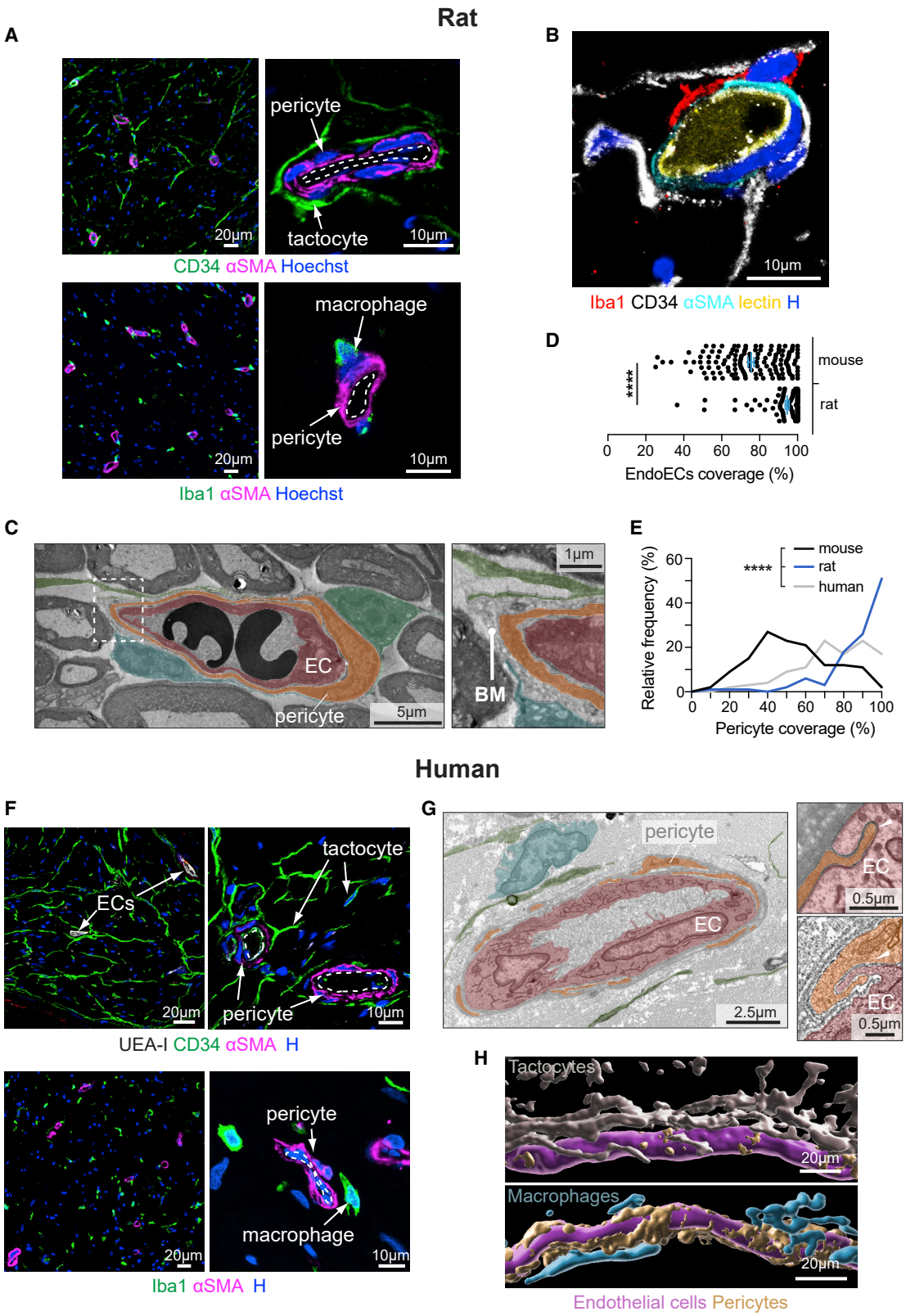

Figure 3. The vascular unit of the PNS is similar across organisms and nerve types

(A) Representative confocal images of transverse sections of rat sciatic nerves labeled to detect pericytes (αSMA, magenta), tactocytes (CD34, green), and macrophages (Iba1, green).

(legend continued on next page)

vascular unit in peripheral nerves implying the importance of this cellular structure in conferring barrier function.

The BNB is conferred by specialized tight junctions and low levels of transcytosis

In the CNS, endothelial barrier function is conferred by specialized TJs that prevent paracellular flux between the ECs and extremely low levels of transcytosis across the ECs.[53] To determine the nature of the BNB in the PNS, we injected horseradish peroxidase (HRP) into the tail veins of mice and used EM to determine EndoEC permeability. We compared EndoBVs, which have barrier function, with EpiBVs, which do not, to detect properties associated with barrier function rather than tissue differences (Figure 1A). EndoEC junctions appeared impermeable to HRP, with a "kissing point" very close to the inner surface of the ECs, similar to those of the BBB[54] (Figures 4A and S4A, quantified in 4B). By contrast, the junctions of EpiECs appeared more permeable, with HRP detected along their length. Consistent with this functional analysis, we detected the differential expression of junctional proteins associated with the specialized TJs of the BBB (Figures 4C and S4B).[53] Specifically, we found occludin, a key structural component of the TJs of the BBB, was detectable at EndoEC TJs but was absent in EpiECs and that claudin-5, the most enriched TJ protein of the BBB, was expressed at EC TJs in all EndoBVs but in a much lower proportion of EpiBVs (<20%). In contrast, the junctional proteins VE-cadherin and ZO1 were expressed similarly in vessels with and without barrier function.

Analysis of nerves from HRP-injected animals also revealed that levels of transcytosis were lower in EndoECs compared with EpiECs, as measured by both the number and density of HRP-containing vesicles within the ECs (Figures 4D–4G and S4A). Low levels of transcytosis are consistent with barrier function; however, the levels appeared higher than those of the BBB in which transcytotic vesicles are rarely detectable.[55,56] Instead, they more closely resembled those of the blood-retinal barrier (BRB),[6] which is consistent with a higher permeability compared with the BBB.[31–33] Transcytosis is associated with the expression of plasmalemma vesicle-associated protein (PLVAP/PV-1), a protein involved in the stabilization of caveolae, transcellular channels, and the formation of fenestrae.[57] PLVAP is not expressed in CNS vessels but becomes upregulated when the barrier is disrupted in pathologies such as cancer.[58–60] Consistent with the low levels of transcytosis in EndoECs, we found that PLVAP was not detectable in EndoECs. In contrast, the vast majority of EpiBVs (82%) were studded with PLVAP (Figures 4H–4I and S4C). Of note, PLVAP- EpiBVs were Claudin+ and likely represent a distinct type of vessel (Figures 4H and S4C). Together, these results showed that, similarly to the CNS, blood barrier function in the PNS is associated with specialized TJs between ECs and by the maintenance of low levels of transcytosis.

Schwann cells increased permeability of the BNB is associated with higher levels of transcytosis

In the PNS, the BNB can be regulated in that the barrier opens following an injury, coincident with the inflammatory response that is important for nerve regeneration.[38,39] In previous work, we showed that the opening of the BNB was orchestrated by SCs.[38,61] Following an injury, SCs are "reprogramed" to a progenitor-like state driven by sustained signaling through the ERK-signaling pathway.[38,62–64] We developed a transgenic mouse model that could mimic this process by inducing elevated ERK-signaling specifically in myelinating SCs (mSCs) (P0-RafTR mice).[38] Using this model, we showed that activation of ERK-signaling in mSCs was sufficient to open the BNB (Figure 5A) providing a powerful model to study the mechanisms by which a blood barrier can be opened in a regulated fashion. To determine the processes by which SCs open the BNB, we analyzed changes in the two components of the BNB following opening of the barrier in the P0-RafTR mouse model. Analysis of the perineurium showed minimal structural changes by EM (Figure S5B), and the immunostaining of junctional proteins (VE-cadherin and ZO1) showed that junctions between the perineurial cells appeared unchanged (Figure S5C). Consistent with no structural changes, we found the functional integrity of the perineurium was unchanged, demonstrating that the perineurial barrier remained intact following the SC-mediated opening of the BNB (Figures S5D and S5E).

We next analyzed EndoBVs. An EM analysis showed that EC morphology changed following the opening of the barrier, in that they appeared less compact and projected more protrusions into the lumen (Figures S5A, S5F, and S5G). To determine changes to the permeability of the EndoBVs, we first analyzed the TJs and found no increase in the permeability of the TJs when the barrier was opened, as measured by the EM analysis of HRP permeability (Figures 5B–5C). Consistent with this, we did not detect changes in

(B) Representative confocal image of the vascular unit in rat sciatic nerve. The lumen is visualized with lectin (yellow), pericytes (αSMA, cyan), tactocytes (CD34, white), and macrophages (Iba1, red).
(C) Representative TEM images of EndoECs (red) and contacting cells in rat sciatic nerves. Pericytes (orange), identified by their localization within the BM, and other cells (blue) were more loosely associated with the blood vessel.
(D) Quantification of EndoEC coverage determined from TEM images of mouse and rat sciatic nerves. Each dot represents a BV, mean ± SEM rat 94.58% ± 1.026%, mouse 75.52% ± 1.546% (n = 3 rats and n = 4 mice. Mann-Whitney p value < 0.0001).
(E) Graph shows the frequency distribution of pericyte coverage calculated from EM images (n = 134 BVs from 6 mice and n = 109 BVs from 3 rats and n = 109 BVs from 3 human samples). Mean pericyte coverage ± SEM: mouse 53.3% ± 1.80%, rat 87.6% ± 1.58%, human 74.41% ± 1.85%. Kruskal-Wallis multiple comparisons of the three means, p value < 0.0001).
(F) Representative confocal images of human endoneurial vasculature showing pericytes (αSMA, magenta) closely associated with EndoECs (UEA-I or white dotted lines). Tactocytes (CD34, green, upper) and macrophages (Iba1, green, lower) are found in looser contact.
(G) Representative array tomography (AT)-SEM images of human EndoECs (red) and contacting cells. Pericytes (orange) were within the BM, whereas other cells were more loosely associated. Insets show snapshots of reciprocal peg-socket interactions (arrowheads) identified from AT-SEM analysis.
(H) Representative 3D-surface reconstructed image of a longitudinal human peripheral nerve section using antibodies to detect ECs (CD31, purple), pericytes (αSMA, orange), tactocytes (CD34, gray, upper panel), and macrophages (Iba1, blue, lower panel) associating along the vessel.
See also Figure S3.

Please cite this article in press as: Malong et al., Characterization of the structure and control of the blood-nerve barrier identifies avenues for therapeutic delivery, Developmental Cell (2023), https://doi.org/10.1016/j.devcel.2023.01.002

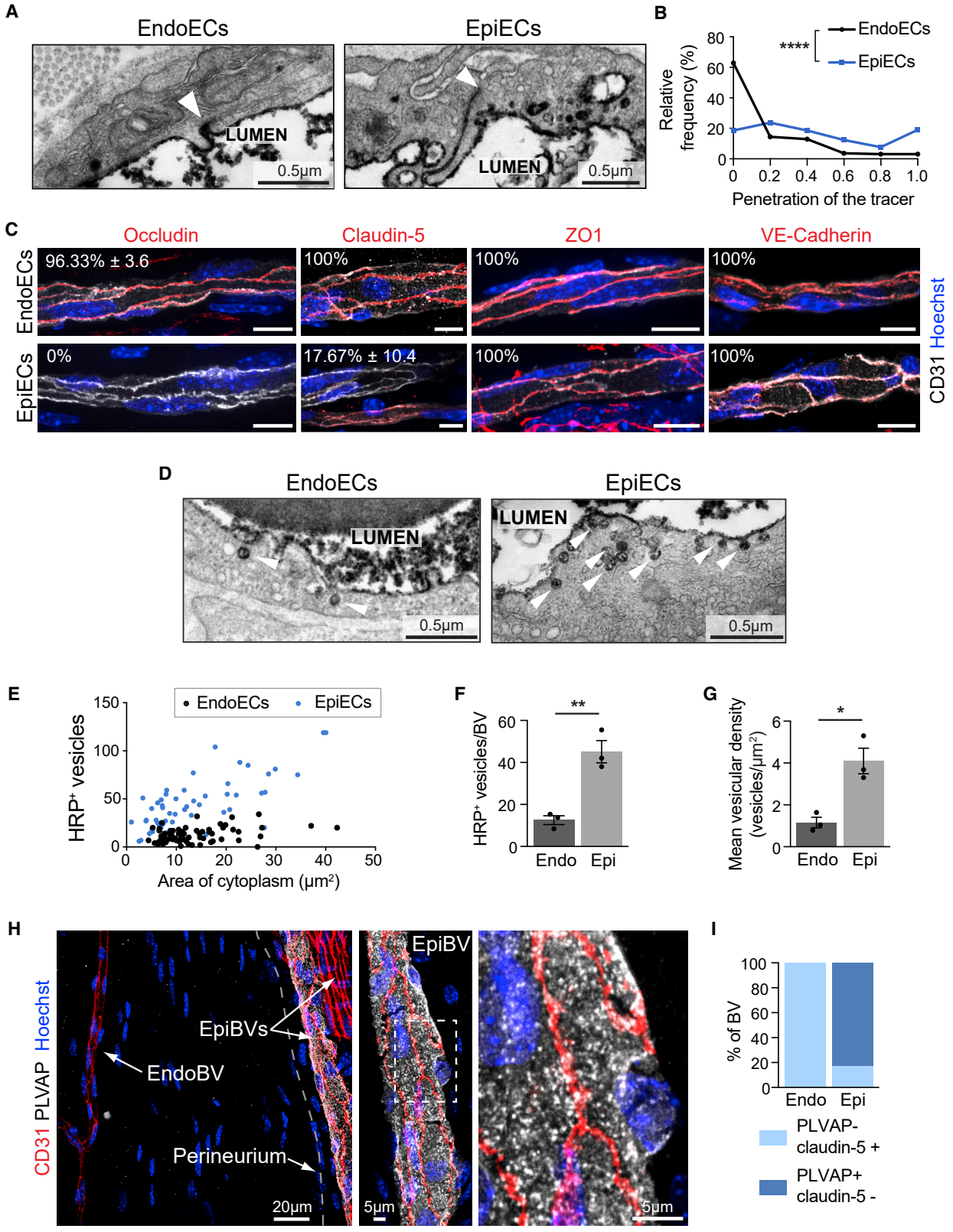

Figure 4. BNB function is conferred by tight junctions and low levels of transcytosis

(A) Representative TEM images of EndoECs and EpiECs from mouse sciatic nerves harvested 5 min following intravenous injection of HRP. White arrowheads indicate penetration of HRP into TJs.

(legend continued on next page)

the expression of junctional proteins (Figures 5D and S5H). In contrast, we found an increase in transcytosis levels when the barrier opened, as measured by both EM analysis of HRP+--transcytotic vesicles (Figures 5E–5H) and immunofluorescence analysis of a second tracer, BSA-FITC (Figures 5I–5J). Consistent with an increase in transcytosis, we observed the upregulation of PLVAP in all EndoBVs (Figures 5K–5L) along with an increase in caveolin-1 (Figures 5M–5N). Together, these results demonstrated that the "opening" of the BNB appears independent of changes to the perineurium or the TJs of EndoECs but is instead associated with increased transcytosis by EndoECs. Importantly, we showed the opening of the barrier was reversible. Following the removal of tamoxifen, the SCs redifferentiate and the animals regain function.[38] In parallel, we found BNB function returned, as measured by Evans blue permeability and PLVAP levels returned to basal levels consistent with reconstituted barrier status (Figure S5I). To determine if changes to the vascular unit were responsible for the opening of the BNB, we analyzed the composition of the vascular unit following opening of the barrier. EM analysis showed the degree of pericyte coverage remained unchanged (Figures S5J and S5K). Moreover, tactocytes also remained associated with the blood vessels at similar levels (Figures S5L and S5M). In contrast, we detected a decrease in the number of macrophages associated with EndoBVs, when the BNB was opened (Figures 5O and S5N; Video S6), despite a large increase in the number of macrophages within the nerve, indicating a potential role for macrophages in barrier function.

Macrophages enforce the BNB

To determine if macrophages confer barrier function, we used a well-characterized pharmacological approach to deplete macrophages from peripheral nerves. This involved treating mice with PLX5622 that targets the CSF1-R, required for macrophage survival and proliferation, and has been shown to efficiently deplete macrophages and microglia from the nervous system.[65,66] Following the administration of PLX5622 for 11–12 days, we found an almost complete (>90%) depletion of macrophages from peripheral nerves, whereas the levels of tactocytes and pericytes were unaffected (Figures 6A and S6A). However, we found that the depletion of macrophages did not appear to affect barrier function, as we did not detect increases in TJ permeability or transcytosis within the EndoECs indicating that macrophages were not responsible for the tightness of the BNB (Figures 6B-6C, and S6B-S6C). Furthermore, the permeability of the perineurium was also unchanged in macrophage-depleted nerves, demonstrating that both components of the BNB remained functional in the absence of macrophages (Figures S6D and S6E).

While performing these experiments, we observed that macrophages rapidly engulfed any HRP that leaked across the BNB in control animals, with levels continuing to accumulate in a time-dependent fashion (Figure 6D). Strikingly, pericytes, tactocytes, and nearby SCs failed to accumulate any detectable HRP indicating a process specific to macrophages (Figures 6E and 6F). A similar uptake of other fluorescent tracers (40 kDa dextran-FITC and BSA-FITC) by macrophages was also observed (Figures 6G, S6F, and S6G), whereas no such leakage or uptake by microglia was observed in the brain (Figure S6G). The process was also conserved in rats, with resident macrophages accumulating leaked HRP within the endoneurium of rat sciatic nerves (Figure S6H).

The efficient "vacuuming" of material that enters the endoneurium suggested that the increased permeability of the BNB may be compensated for by macrophages, providing an additional mechanism to protect the nerve environment. Consistent with this hypothesis, we detected the accumulation of HRP throughout the endoneurium of macrophage-depleted nerves. The leakage of HRP into the endoneurium could be observed by eye, in nerves depleted of macrophages when stained for HRP reactivity (Figure 6H, left). Fluorescence microscopy showed that in contrast to control nerves, where HRP was detectable only within the blood vessels and macrophages, nerves lacking macrophages showed high levels of HRP throughout the endoneurium (Figure 6H, middle). Quantification showed the area of HRP staining was ~24% of the endoneurium (Figure S6I), corresponding to the known intrafascicular space,[67] consistent with the spread of leaked material throughout the endoneurium. EM analysis confirmed this finding, with HRP detected in the spaces between mSCs, obscuring collagen bundles seen in control nerves (Figure 6H, right). Similar results were obtained with a second tracer, 10kDa dextran-FITC (Figures S6J and S6K). These findings indicate that macrophages provide a secondary barrier to enforce the protection provided by the ECs to further protect the nerve environment from blood-borne molecules.

Increasing the permeability of the BNB can improve drug delivery to the PNS

The BNB is thought to be important to maintain the PNS microenvironment, but it also hinders therapeutic delivery.[34] Identifying that the BNB can be reversibly regulated by SCs and the role of macrophages in enforcing the barrier provides potential

(B) Graph shows the relative frequency distribution of the penetration of HRP into the junctions of EndoECs (black) and EpiECs (blue) (n = 55/52 BVs and 194/194 junctions from 3 mice, mean ± SEM: EndoBVs 0.16 ± 0.018, EpiBVs 0.45 ± 0.025, Mann-Whitney comparison of the means, p value < 0.0001).
(C) Representative iSIM fluorescent images of longitudinal sections of EndoBVs and EpiBVs from mouse sciatic nerves stained for indicated junctional proteins (red). Percentages indicate mean ± SEM of positive BVs (EndoBVs/EpiBVs from 3 mice: claudin-5 n = 25/22, occludin n = 54/33, ZO1 n = 43/31, VE-cadherin n = 39/32). Scale bars, 10 μm.
(D) Representative TEM images of EndoECs and EpiECs of mouse sciatic nerves harvested 5 min following intravenous injection of HRP. White arrowheads indicate HRP+ vesicles.
(E) Quantification of (D). Each dot represents a blood vessel (n = 3 mice).
(F) Graph shows the mean number of HRP+ vesicles ± SEM per blood vessel as represented in (E), unpaired t test p value = 0.0046.
(G) Graph shows the mean vesicular density ± SEM, as represented in (E), unpaired t test p value = 0.0112.
(H) Representative confocal images showing longitudinal sections of mouse sciatic nerve stained for PLVAP (white) and CD31 (red). The perineurium is shown by a dashed line. Right panels show zoomed images of a EpiBV showing punctate staining of PLVAP.
(I) Graph shows the percentage of EndoBVs and EpiBVs that are positive for PLVAP and claudin-5 (n = 25 EndoBVs and 22 EpiBVs from 3 mice).
See also Figure S4.

Please cite this article in press as: Malong et al., Characterization of the structure and control of the blood-nerve barrier identifies avenues for therapeutic delivery, Developmental Cell (2023), https://doi.org/10.1016/j.devcel.2023.01.002

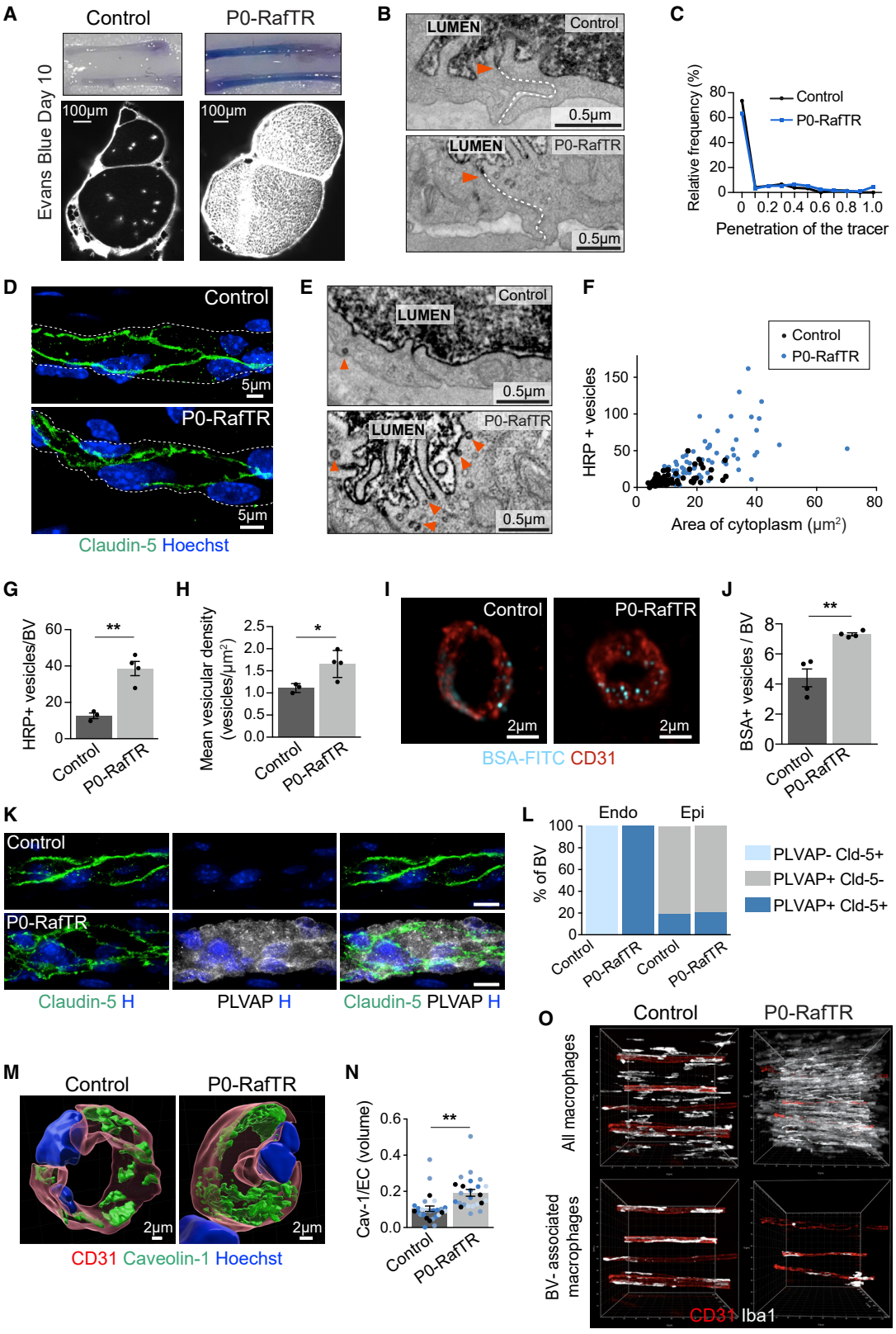

Figure 5. Schwann cells increased permeability of the BNB is associated with higher levels of transcytosis

(A) Mouse sciatic nerves from control and P0-RafTR mice, day 10 after the first administration of tamoxifen, injected with Evans blue, prior to harvest. Upper panel shows light images of intact nerves. Lower panel shows fluorescent images of transverse sections showing Evans blue (white).

(legend continued on next page)

Please cite this article in press as: Malong et al., Characterization of the structure and control of the blood-nerve barrier identifies avenues for therapeutic delivery, Developmental Cell (2023), https://doi.org/10.1016/j.devcel.2023.01.002

mechanisms to increase drug delivery to the PNS. Antisense oligonucleotides (ASOs) are short, single-stranded DNA molecules that are designed to modify specific and often pathogenic gene expression.[68] ASOs are potentially powerful therapeutics for the nervous system and are showing promise for the treatment of diseases such as muscular dystrophy and Huntington's disease.[69,70] However, blood neural barriers act as a major limiting factor for delivery to these tissues.[68,71–73]

To determine the effects of opening the barrier on the ability to deliver ASOs into the endoneurium of peripheral nerves, we analyzed the uptake of ASOs conjugated to Cy3 into peripheral nerves, permitting both a quantitative analysis of uptake and the visualization of the mechanisms involved. We injected ASOs targeting the long non-coding RNA Malat1 into the tail vein of tamoxifen-treated control and P0-RafTR animals at a time point when the BNB is open in the P0-RafTR mice. Consistent with the BNB providing a barrier to ASO uptake in control animals, the majority of ASO-associated fluorescence was retained outside of the endoneurium, with expression restricted to macrophages within the endoneurium (Figures 7A–7C). By contrast, in P0-RafTR animals, ASO-associated fluorescence could be detected at high levels throughout the endoneurium, rapidly (10 min) and over a sustained period, following a single injection (Figures 7A–7C) with high levels of fluorescence observed in most cells within the endoneurium (Figures 7C and 7D). Importantly, as many therapeutics would aim to target SCs, we could detect high levels of the fluorescent ASO within mSCs (Figures 7E and 7F). Consistent with increased levels of transcytosis being responsible for the opening of the BNB, the labeled ASO was detected within vesicular structures within the cytoplasm of ECs (Figures 7G and 7H and quantified in 7I). Consistent with increased levels of ASO within the nerves of P0-RafTR mice, there was a greater decrease of Malat1 RNA levels in the nerves of these mice (Figure 7J). These results demonstrate the potential of manipulating the BNB to improve therapeutic delivery to the PNS.

DISCUSSION

The endoneurium of peripheral nerves is a protected environment enforced by the BNB. Here, we define the cellular structure that provides this protection and shows that it differs markedly from the well-defined vascular unit that constitutes the BBB. In contrast to vessels in the CNS, the endothelium of blood vessels in the PNS is only partially covered by other cell types, and these cell types are different from those that envelop the endothelium in the CNS. Pericyte coverage appears somewhat similar to the CNS[23,74] and tactocytes and macrophages provide additional coverage instead of the astrocyte coverage observed in the CNS. Interestingly, although the overall cellular coverage of the endothelium is lower in the PNS, our 3D analysis showed that each cell type makes some contact with the majority of ECs along individual blood vessels, indicating that each cell type may contribute to barrier function. The distinctive multicellular structure of the BNB vascular unit is conserved within the mouse and in both rat and human peripheral nerves. This conservation of the vascular unit of the PNS between nerve types and species argues the importance of this multicellular structure in conferring barrier function and our findings on the differences to the BBB are an important step to understanding and manipulating these distinct barriers.

In the CNS, the barrier function of the endothelium is conferred by signals from both pericytes and astrocytes.[24–26,75–77] In PNS vessels, the high level of pericyte coverage makes it likely that pericytes have a similar role in conferring barrier function, though this remains to be tested. However, astrocytes do not exist in peripheral nerves so interactions with other cell types are likely to be important. Macrophages do not appear to be involved, as we found that the depletion of macrophages had no effect on the permeability of the primary barrier. In contrast, tactocytes are good candidates to confer barrier function. These poorly characterized cells have a distinct morphology, exhibiting multiple, long, thin protrusions that interact with multiple cell types within the endoneurium.[44] Moreover, they exhibit extensive, direct endfeet-like contacts with the BM of EndoBVs indicative of a signaling role and resembling aspects of astrocyte biology. This suggests that tactocytes may act as astrocytes of the PNS and may therefore have important roles in the development and/or maintenance of barrier function in the PNS. Further work is needed to better understand this cell type and characterize the nature of their interactions in peripheral nerves.

(B) Representative TEM images of indicated mice treated with tamoxifen for 10 days and injected with HRP prior to harvest. Orange arrowheads indicate penetration of HRP into the EC junctions (white dotted lines).
(C) Quantification of (B), (Ctrl/P0-RafTR n = 3/4 mice, 79/45 BVs, and 212/240 junctions).
(D) Representative confocal images showing longitudinal sections of EndoBVs (white dotted outline) of control and P0RafTR (day 10), stained for claudin-5 (green).
(E) Representative TEM images of indicated mice treated with tamoxifen for 10 days and injected with HRP prior to harvest. HRP+ vesicles are marked by orange arrowheads.
(F) Quantification of (E). Each dot represents a blood vessel from 3 controls and 4 P0-RafTR mice.
(G) Graph shows the mean number of HRP+ vesicles per blood vessel ± SEM from (F). t test p value = 0.0028.
(H) Graph shows the mean vesicular density ± SEM from (F). t test p value = 0.0331.
(I) Representative confocal images of EndoBVs from indicated mice (day 10), injected with BSA-FITC, 6 h prior to harvest and stained for CD31 (red).
(J) Quantification of (I). n = 4 mice per group. t test p value = 0.003.
(K) Representative iSIM super-resolution images showing longitudinal sections of sciatic nerves from indicated mice (day 10) stained for claudin-5 (green) and PLVAP (white). Scale bars, 10 μm.
(L) Quantification of (K), (n = 16 EndoBV and 27 EpiBV from 3 control mice and n = 48 EndoBV and 38 EpiBV from 5 P0-RafTR mice).
(M) Representative 3D-surface-reconstructed, super-resolution image of an EndoBV from indicated mice (day 10), stained for caveolin-1 (green) and CD31 (red).
(N) Quantification of (M). Different shades of blue represent the 4 mice analyzed. Each dot represents an EndoEC, mean ± SEM (unpaired t test p value = 0.0055).
(O) Representative confocal images showing the localization of macrophages (white) in the endoneurium of iDISCO-cleared mouse sciatic nerves from indicated mice (day 10). Upper panels show all macrophages, lower panels only EndoBV-associated macrophages. See Video S6.
See also Figure S5.

Please cite this article in press as: Malong et al., Characterization of the structure and control of the blood-nerve barrier identifies avenues for therapeutic delivery, Developmental Cell (2023), https://doi.org/10.1016/j.devcel.2023.01.002

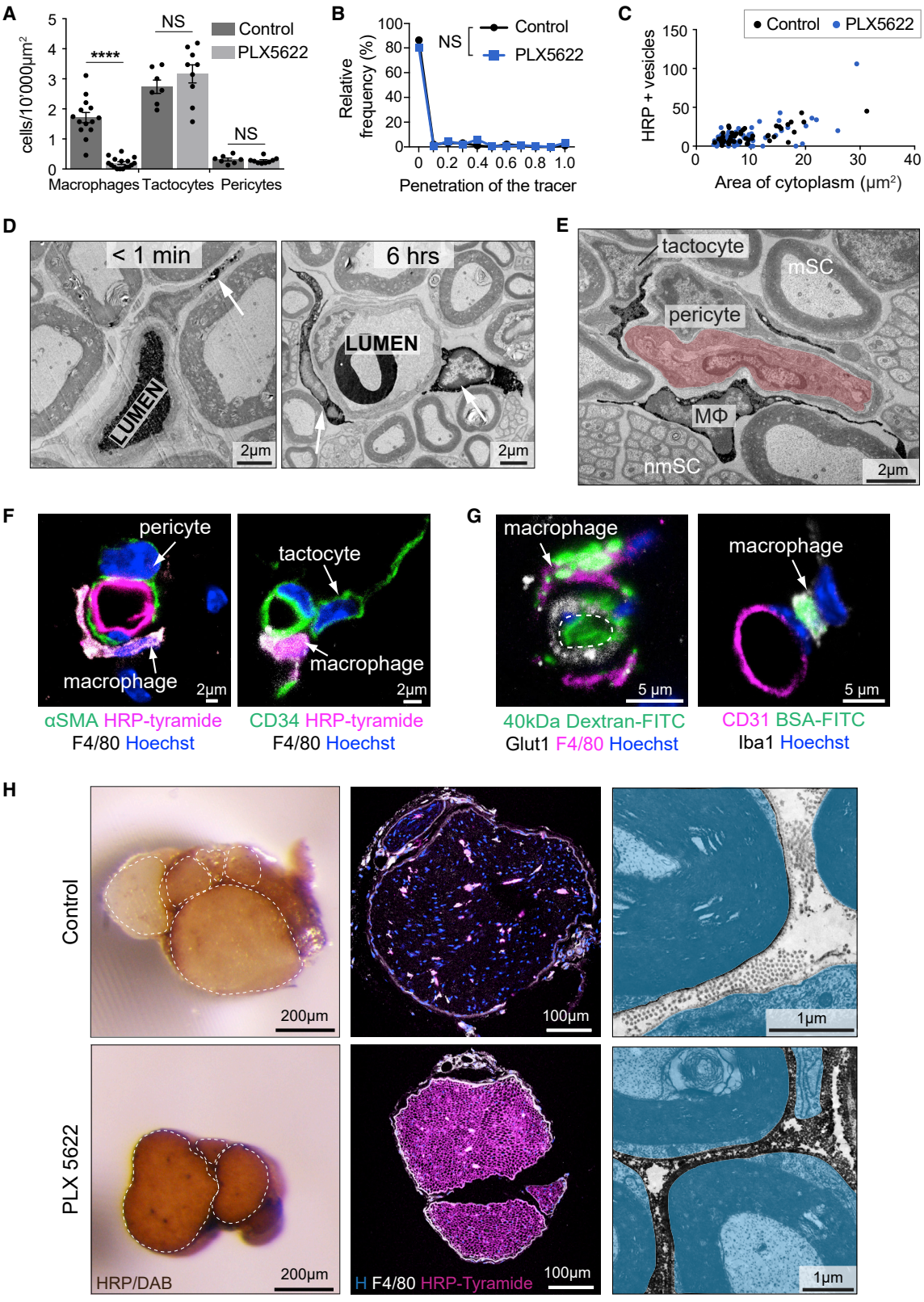

(legend on next page)

Similarly to blood vessels in the CNS, we found that ECs in peripheral nerves have specialized cell:cell junctions that inhibit leakage between the cells, together with low levels of transcytosis. However, transcytosis levels were higher than those in the CNS but similar to those found associated with the BRB consistent with the "leakier" nature of both the BRB and the BNB.[6] Why the neural environments of the PNS and the retina appear to require less protection remains unclear—it could reflect that these nerve types are less sensitive to some leakage or perhaps permits the transport of substances needed for their distinct environments and/or reflects the different requirements of supporting axons at greater distances from their cell bodies. Importantly, however, we found that this "leaked" material was rapidly cleared from the endoneurium by macrophages. Macrophages do not appear to confer barrier function. Instead, macrophages appear to act as a second line of defense by vacuuming up material that crosses the barrier. This role of macrophages in enforcing barrier function implies that aspects of this "leakage" could have detrimental effects on the endoneurial environment. Uptake into macrophages is rapid, specific, and efficient, in that in the absence of macrophages, leaked material rapidly accumulates to fill the endoneurial space, implying an important role in maintaining the protected environment of the endoneurium. This homeostatic role becomes overwhelmed once the barrier is opened, resulting in the uptake of substances by other cell types—emphasizing their unique role in clearing leaked material and potential therapeutic avenues.

Many disorders of the PNS have been associated with defects in the BNB, such as diabetic neuropathies, pain, and neurodegeneration. However, the mechanisms underlying the pathologies remain relatively poorly understood.[36,37,78] Our findings and tools should provide a platform to address the role of the BNB in these various pathologies. In addition, a great advantage of our model system (P0-RafTR mice) is that we can reversibly "open" the BNB in the absence of trauma, which simplifies the analysis of mechanisms by which the barrier can be controlled. Using this model, we found that transport across the endothelium was associated with higher levels of transcytosis without any change to the permeability of the TJs. This was coincident with the upregulation of PLVAP expression in all EndoBVs, reflective of a switch to an "open" endothelium in all vessels within the nerve. Little is known about the cargos of transcytotic vesicles and whether they exhibit selected transport.[79] We found that all tracers we tested were transported by transcytotic vesicles; moreover, we found that ASOs delivered to the blood were also transported across ECs by this route, highlighting the potential to temporarily upregulate these pathways to improve drug delivery to the nervous system.

Limitations of the study

The signals by which SCs increase transcytosis rates in ECs have not been identified and will be the focus of future studies. Moreover, these findings may not be directly translatable because of associated demyelination and potential inflammatory responses, together with the non-specificity of the molecules transported; however, this work provides new approaches and targets toward a therapeutic goal.

STAR★METHODS

Detailed methods are provided in the online version of this paper and include the following:

- KEY RESOURCES TABLE
- RESOURCE AVAILABILITY
  - Lead contact
  - Materials availability
  - Data and code availability
- EXPERIMENTAL MODELS AND SUBJECT DETAILS
  - Rodent husbandry
  - Human tissue
- METHOD DETAILS
  - Administration of substances
  - qRT-PCR
  - Immunofluorescence
  - 3D immunostaining
  - Transmission Electron Microscopy (TEM)
  - Serial Block Face SEM (SBF-SEM)
  - Array Tomography SEM (AT-SEM)
  - Correlative light electron microscopy (CLEM)

Figure 6. Macrophages enforce the BNB

(A) Quantification of Figure S6A showing macrophage (F4/80+), tactocyte (CD34+), and pericyte (αSMA+) number in the endoneurium of mice treated with control (dark gray) or PLX5622 (light gray) containing chow. Mean ± SEM, n = 14/16 mice for macrophages and 7/9 mice for pericytes and tactocytes. t test p values 0.2978 for tactocytes and 0.5460 for pericytes and p value < 0.0001 for macrophages.

(B) Quantification of the permeability of TJs in control and PLX5622 treated mice from TEM images (Figure S6B), n = 5 control and 6 PLX5622 mice, mean ± SEM: control 0.05 ± 0.017, PLX5622 0.095 ± 0.019, Mann-Whitney comparison of the two means p value = 0.0529.

(C) Quantification of (Figure S6B), transcytosis levels in control (black) and PLX5622 treated (blue) mice. Each dot represents an individual blood vessel (n = 5 control and 6 PLX5622 mice).

(D) Representative TEM images of mouse sciatic nerves following the intravenous injection of HRP and harvested immediately (<1 min) and 6 h later. White arrows point to macrophages containing HRP.

(E) Representative TEM image of mouse sciatic nerves following the intravenous injection of HRP and harvested 6 h later. Only macrophages (MΦ) accumulated HRP.

(F) Representative confocal images of mouse sciatic nerves following the intravenous injection of HRP and harvested 6 h later. Only macrophages accumulated HRP.

(G) Representative confocal images of mouse sciatic nerves following the intravenous injection of 40 kDa dextran-FITC (green, left panel) or BSA-FITC (green, right panel) and harvested 6 h later.

(H) Left: representative images of 150 μm thick nerve sections stained with 3,3-diaminobenzidine (DAB) from indicated mice. Middle: confocal images of tyramide reactivity (magenta). Right: TEM images of HRP accumulation in the endoneurial space. Cells are colored blue.

See also Figure S6.

Please cite this article in press as: Malong et al., Characterization of the structure and control of the blood-nerve barrier identifies avenues for therapeutic delivery, Developmental Cell (2023), https://doi.org/10.1016/j.devcel.2023.01.002

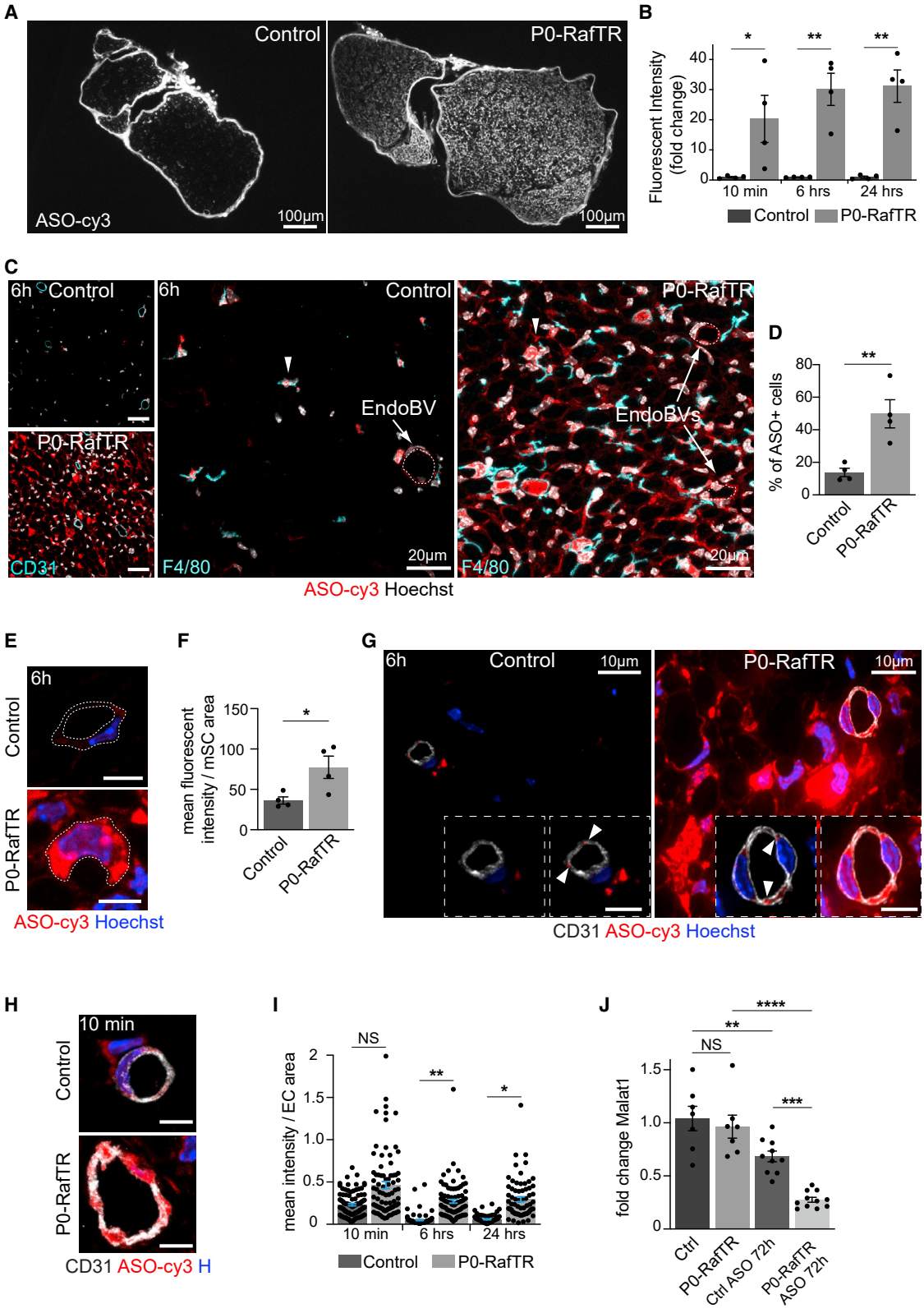

Figure 7. Increasing the permeability of the BNB can improve drug delivery to the PNS

(A) Representative fluorescent image of ASO-cy3 (white) distribution in transverse sections of the sciatic nerve, 10 min following intravenous injection into indicated mice, day 10 after first tamoxifen administration.

(legend continued on next page)

- Assessment of BNB function by Evans Blue
- Assessment of the permeability of the perineurium
- Light Microscope details
- Experimental Design
- QUANTIFICATION AND STATISTICAL ANALYSIS
  - Image quantification
  - Statistical analysis

SUPPLEMENTAL INFORMATION

Supplemental information can be found online at https://doi.org/10.1016/j.devcel.2023.01.002.

ACKNOWLEDGMENTS

This study was supported by an MRC grant, MR/N009169/1, CRUK programme grant (C378/A28282), a WT PhD-studentship to L.M., MRC core funding, MC_U12266B, and WT funding (218278/Z/19/Z) for the acquisition of the AT-SEM. We thank UCL Biological Services, Plexxikon Inc. for the PLX5622-formulated chow, Peter Munro for the assistance with SBF-SEM, and Lenn Tchern for the assistance with Imaris.

AUTHOR CONTRIBUTIONS

L.M., I.N., and A.C.L. conceived and designed the project. L.M., I.N., G.C., I.J.W, S.S., A.-L.C., J.J.B., A.B., and K.I.H. performed the experiments. A.F. provided the human material. H.T.Z. provided the ASOs and collaborative advice. L.M., G.C., and A.C.L. wrote the manuscript and made the figures. All authors reviewed the manuscript.

DECLARATION OF INTERESTS

The authors declare no competing interests.

Received: February 22, 2022
Revised: October 26, 2022
Accepted: January 4, 2023
Published: January 26, 2023

REFERENCES

1. Aird, W.C. (2007). Phenotypic heterogeneity of the endothelium: I. Structure, function, and mechanisms. Circ. Res. *100*, 158–173. https://doi.org/10.1161/01.RES.0000255691.76142.4a.
2. Kalucka, J., de Rooij, L.P.M.H., Goveia, J., Rohlenova, K., Dumas, S.J., Meta, E., Conchinha, N.V., Taverna, F., Teuwen, L.A., Veys, K., et al. (2020). Single-cell transcriptome atlas of murine endothelial cells. Cell *180*. 764–779.e20. https://doi.org/10.1016/j.cell.2020.01.015.
3. Shetty, S., Lalor, P.F., and Adams, D.H. (2018). Liver sinusoidal endothelial cells - gatekeepers of hepatic immunity. Nat. Rev. Gastroenterol. Hepatol. *15*, 555–567. https://doi.org/10.1038/s41575-018-0020-y.
4. Daneman, R., and Prat, A. (2015). The blood-brain barrier. Cold Spring Harb. Perspect. Biol. *7*, a020412. https://doi.org/10.1101/cshperspect.a020412.
5. Liebner, S., Dijkhuizen, R.M., Reiss, Y., Plate, K.H., Agalliu, D., and Constantin, G. (2018). Functional morphology of the blood–brain barrier in health and disease. Acta Neuropathol. *135*, 311–336. https://doi.org/10.1007/s00401-018-1815-1.
6. Chow, B.W., and Gu, C. (2017). Gradual suppression of transcytosis governs functional blood-retinal barrier formation. Neuron *93*. 1325–1333.e3. https://doi.org/10.1016/j.neuron.2017.02.043.
7. Weiss, N., Miller, F., Cazaubon, S., and Couraud, P.O. (2009). The blood-brain barrier in brain homeostasis and neurological diseases. Biochim. Biophys. Acta *1788*, 842–857. https://doi.org/10.1016/j.bbamem.2008.10.022.
8. Pardridge, W.M. (2005). The blood-brain barrier: bottleneck in brain drug development. Neurorx *2*, 3–14.
9. Zhao, Z., Nelson, A.R., Betsholtz, C., and Zlokovic, B.V. (2015). Establishment and dysfunction of the blood-brain barrier. Cell *163*, 1064–1078. https://doi.org/10.1016/j.cell.2015.10.067.
10. van Deurs, B. (1980). Structural aspects of brain barriers, with special reference to the permeability of the cerebral endothelium and choroidal epithelium. Int. Rev. Cytol. *65*, 117–191.
11. Gross, B., Bitterman, N., Levanon, D., Nir, I., and Harel, D. (1986). Horseradish peroxidase as a cytochemical marker of blood-brain barrier integrity in oxygen toxicity in the central nervous system. Exp. Neurol. *93*, 471–480. https://doi.org/10.1016/0014-4886(86)90168-8.
12. Lajoie, J.M., and Shusta, E.V. (2015). Targeting receptor-mediated transport for delivery of biologics across the blood-brain barrier. Annu. Rev. Pharmacol. Toxicol. *55*, 613–631. https://doi.org/10.1146/annurev-pharmtox-010814-124852.
13. Villaseñor, R., Lampe, J., Schwaninger, M., and Collin, L. (2019). Intracellular transport and regulation of transcytosis across the blood–brain barrier. Cell. Mol. Life Sci. *76*, 1081–1092. https://doi.org/10.1007/s00018-018-2982-x.
14. Daneman, R., Zhou, L., Agalliu, D., Cahoy, J.D., Kaushal, A., and Barres, B.A. (2010). The mouse blood-brain barrier transcriptome: a new resource for understanding the development and function of brain endothelial cells. PLoS One *5*, e13741. https://doi.org/10.1371/journal.pone.0013741.
15. Huntley, M.A., Bien-Ly, N., Daneman, R., and Watts, R.J. (2014). Dissecting gene expression at the blood-brain barrier. Front. Neurosci. *8*, 355. https://doi.org/10.3389/fnins.2014.00355.
16. Vanlandewijck, M., He, L., Mäe, M.A., Andrae, J., Ando, K., Del Gaudio, F., Nahar, K., Lebouvier, T., Laviña, B., Gouveia, L., et al. (2018). A molecular

(B) Quantification of (A) at the indicated time points (ASO-cy3, n = 4 control, and 4 P0-RafTR mice. t test values 10 min: p = 0.0484, 6 h: p = 0.0016, and 24 h: p = 0.0014).
(C) Representative confocal images of ASO-cy3 within the endoneurium of sciatic nerves of indicated mice, 6 h following a single intravenous injection of ASO-cy3 (red). LHS: EndoECs CD31 (cyan). Scale bars, 20 μm. RHS: macrophages, F4/80 (cyan) are indicated by arrowheads. EndoBVs are indicated by dotted lines and arrows.
(D) Quantification of (C), mean ± SEM, n = 4 control and 4 P0-RafTR mice. t test p value = 0.0073.
(E) Representative confocal images of (C) showing the accumulation of ASO-cy3 (red) in mSCs, 6 h after ASO intravenous injection. Scale bars, 5 μm.
(F) Quantification of (E), (control n = 91 SCs and P0-RafTR n = 108 SCs from 4 mice, t test p = 0.0302).
(G) Representative iSIM super-resolution images of sciatic nerves from indicated mice (day 10), injected with ASO-cy3 and harvested 6 h later. Insets show higher magnifications of individual EndoBVs (arrows) with (left) non-saturated ASO-cy3 signal and (right) saturated ASO-cy3 signal to visualize vesicles (arrowheads) in controls. Scale bars, 5 μm.
(H) Representative confocal images 10 min after ASO-cy3 injection. Scale bars, 5 μm.
(I) Quantification of (H) measured at indicated time points (a.u. mean ± SEM: n = 4 mice). Unpaired t test value 10 min = 0.13, 6 h = 0.006, and 24 h = 0.0295.
(J) Graph shows fold change in Malat1 RNA expression normalized to B2M in control and P0-RafTR (day 10) mice, 72 h following the intravenous injection of Malat1 ASO, (mean ± SEM), n = 7 mice in Ctrl and P0-RafTR, n = 10 in Ctrl ASO-injected, and n = 11 in P0-RafTR ASO-injected. ANOVA/Tukey multiple comparison p values: Ctrl vs. P0-RafTR = 0.899, Ctrl vs Ctrl ASO = 0.0076, P0-RafTR vs P0-RafTR ASO <0.0001, Ctrl ASO vs P0-RafTR ASO = 0.0005.

atlas of cell types and zonation in the brain vasculature. Nature *554*, 475–480. https://doi.org/10.1038/nature25739.

17. Stewart, P.A., and Wiley, M.J. (1981). Developing nervous tissue induces formation of blood-brain barrier characteristics in invading endothelial cells: a study using quail-chick transplantation chimeras. Dev. Biol. *84*, 183–192. https://doi.org/10.1016/0012-1606(81)90382-1.
18. Helms, H.C., Abbott, N.J., Burek, M., Cecchelli, R., Couraud, P.O., Deli, M.A., Förster, C., Galla, H.J., Romero, I.A., Shusta, E.V., et al. (2016). In vitro models of the blood-brain barrier: an overview of commonly used brain endothelial cell culture models and guidelines for their use. J. Cereb. Blood Flow Metab. *36*, 862–890. https://doi.org/10.1177/0271678X16630991.
19. Villabona-Rueda, A., Erice, C., Pardo, C.A., and Stins, M.F. (2019). The evolving concept of the blood brain barrier (BBB): from a single static barrier to a heterogeneous and dynamic relay center. Front. Cell. Neurosci. *13*, 405. https://doi.org/10.3389/fncel.2019.00405.
20. Abbott, N.J., Rönnbäck, L., and Hansson, E. (2006). Astrocyte-endothelial interactions at the blood-brain barrier. Nat. Rev. Neurosci. *7*, 41–53. https://doi.org/10.1038/nrn1824.
21. McConnell, H.L., Kersch, C.N., Woltjer, R.L., and Neuwelt, E.A. (2017). The translational significance of the neurovascular unit. J. Biol. Chem. *292*, 762–770. https://doi.org/10.1074/jbc.R116.760215.
22. Sweeney, M.D., Ayyadurai, S., and Zlokovic, B.V. (2016). Pericytes of the neurovascular unit: key functions and signaling pathways. Nat. Neurosci. *19*, 771–783. https://doi.org/10.1038/nn.4288.
23. Mathiisen, T.M., Lehre, K.P., Danbolt, N.C., and Ottersen, O.P. (2010). The perivascular astroglial sheath provides a complete covering of the brain microvessels: an electron microscopic 3D reconstruction. Glia *58*, 1094–1103. https://doi.org/10.1002/glia.20990.
24. Armulik, A., Genové, G., Mäe, M., Nisancioglu, M.H., Wallgard, E., Niaudet, C., He, L., Norlin, J., Lindblom, P., Strittmatter, K., et al. (2010). Pericytes regulate the blood-brain barrier. Nature *468*, 557–561. https://doi.org/10.1038/nature09522.
25. Daneman, R., Zhou, L., Kebede, A.A., and Barres, B.A. (2010). Pericytes are required for blood-brain barrier integrity during embryogenesis. Nature *468*, 562–566. https://doi.org/10.1038/nature09513.
26. Segarra, M., Aburto, M.R., Cop, F., Llaó-Cid, C., Härtl, R., Damm, M., Bethani, I., Parrilla, M., Husainie, D., Schänzer, A., et al. (2018). Endothelial Dab1 signaling orchestrates neuro-glia-vessel communication in the central nervous system. Science *361*, eaao2861. https://doi.org/10.1126/science.aao2861.
27. Armulik, A., Genové, G., and Betsholtz, C. (2011). Pericytes: developmental, physiological, and pathological perspectives, problems, and promises. Dev. Cell *21*, 193–215. https://doi.org/10.1016/j.devcel.2011.07.001.
28. Smith, C.E., Atchabahian, A., Mackinnon, S.E., and Hunter, D.A. (2001). Development of the blood-nerve barrier in neonatal rats. Microsurgery *21*, 290–297.
29. Kristensson, K., and Olsson, Y. (1971). The perineurium as a diffusion barrier to protein tracers. Differences between mature and immature animals. Acta Neuropathol. *17*, 127–138.
30. Kristensson, K. (1970). Transport of fluorescent protein tracer in peripheral nerves. Acta Neuropathol. *16*, 293–300. https://doi.org/10.1007/BF00686894.
31. Allt, G., and Lawrenson, J.G. (2000). The blood-nerve barrier: enzymes, transporters and receptors–a comparison with the blood-brain barrier. Brain Res. Bull. *52*, 1–12.
32. Wadhwani, K.C., and Rapoport, S.I. (1994). Transport properties of vertebrate blood-nerve barrier: comparison with blood-brain barrier. Prog. Neurobiol. *43*, 235–279. https://doi.org/10.1016/0301-0082(94)90002-7.
33. Welch, K., and Davson, H. (1972). The permeability of capillaries of the sciatic nerve of the rabbit to several materials. J. Neurosurg. *36*, 21–26. https://doi.org/10.3171/jns.1972.36.1.0021.
34. Langert, K.A., and Brey, E.M. (2018). Strategies for targeted delivery to the peripheral nerve. Front. Neurosci. *12*, 887. https://doi.org/10.3389/fnins.2018.00887.
35. Liu, H., Chen, Y., Huang, L., Sun, X., Fu, T., Wu, S., Zhu, X., Zhen, W., Liu, J., Lu, G., et al. (2018). Drug distribution into peripheral nerve. J. Pharmacol. Exp. Ther. *365*, 336–345. https://doi.org/10.1124/jpet.117.245613.
36. Richner, M., Ferreira, N., Dudele, A., Jensen, T.S., Vaegter, C.B., and Gonçalves, N.P. (2018). Functional and structural changes of the blood-nerve-barrier in diabetic neuropathy. Front. Neurosci. *12*, 1038. https://doi.org/10.3389/fnins.2018.01038.
37. Staff, N.P., Grisold, A., Grisold, W., and Windebank, A.J. (2017). Chemotherapy-induced peripheral neuropathy: a current review. Ann. Neurol. *81*, 772–781. https://doi.org/10.1002/ana.24951.
38. Napoli, I., Noon, L.A., Ribeiro, S., Kerai, A.P., Parrinello, S., Rosenberg, L.H., Collins, M.J., Harrisingh, M.C., White, I.J., Woodhoo, A., and Lloyd, A.C. (2012). A central role for the ERK-signaling pathway in controlling Schwann cell plasticity and peripheral nerve regeneration in vivo. Neuron *73*, 729–742. https://doi.org/10.1016/j.neuron.2011.11.031.
39. Zochodne, D.W. (2008). Neurobiology of Peripheral Nerve Regeneration (Cambridge University Press).
40. Schaeffer, S., and Iadecola, C. (2021). Revisiting the neurovascular unit. Nat. Neurosci. *24*, 1198–1209. https://doi.org/10.1038/s41593-021-00904-7.
41. Bell, M.A., and Weddell, A.G. (1984). A morphometric study of intrafascicular vessels of mammalian sciatic nerve. Muscle Nerve *7*, 524–534. https://doi.org/10.1002/mus.880070703.
42. Tserentsoodol, N., Shin, B.C., Koyama, H., Suzuki, T., and Takata, K. (1999). Immunolocalization of tight junction proteins, occludin and ZO-1, and glucose transporter GLUT1 in the cells of the blood-nerve barrier. Arch. Histol. Cytol. *62*, 459–469. https://doi.org/10.1679/aohc.62.459.
43. Obermeier, B., Daneman, R., and Ransohoff, R.M. (2013). Development, maintenance and disruption of the blood-brain barrier. Nat. Med. *19*, 1584–1596. https://doi.org/10.1038/nm.3407.
44. Stierli, S., Napoli, I., White, I.J., Cattin, A.L., Monteza Cabrejos, A., Garcia Calavia, N., Malong, L., Ribeiro, S., Nihouarn, J., Williams, R., et al. (2018). The regulation of the homeostasis and regeneration of peripheral nerve is distinct from the CNS and independent of a stem cell population. Development *145*, dev170316. https://doi.org/10.1242/dev.170316.
45. Joseph, N.M., Mukouyama, Y.S., Mosher, J.T., Jaegle, M., Crone, S.A., Dormand, E.L., Lee, K.F., Meijer, D., Anderson, D.J., and Morrison, S.J. (2004). Neural crest stem cells undergo multilineage differentiation in developing peripheral nerves to generate endoneurial fibroblasts in addition to Schwann cells. Development *131*, 5599–5612. https://doi.org/10.1242/dev.01429.
46. Richard, L., Topilko, P., Magy, L., Decouvelaere, A.V., Charnay, P., Funalot, B., and Vallat, J.M. (2012). Endoneurial fibroblast-like cells. J. Neuropathol. Exp. Neurol. *71*, 938–947. https://doi.org/10.1097/NEN.0b013e318270a941.
47. Mirancea, N. (2016). Telocyte – a particular cell phenotype. Infrastructure, relationships and putative functions. Rom J. Morphol. Embryol. *57*, 7–21.
48. Carr, M.J., Toma, J.S., Johnston, A.P.W., Steadman, P.E., Yuzwa, S.A., Mahmud, N., Frankland, P.W., Kaplan, D.R., and Miller, F.D. (2019). Mesenchymal precursor cells in adult nerves contribute to mammalian tissue repair and regeneration. Cell Stem Cell *24*. 240–256.e9. https://doi.org/10.1016/j.stem.2018.10.024.
49. Sidney, L.E., Branch, M.J., Dunphy, S.E., Dua, H.S., and Hopkinson, A. (2014). Concise review: evidence for CD34 as a common marker for diverse progenitors. Stem Cells *32*, 1380–1389. https://doi.org/10.1002/stem.1661.
50. Mueller, M., Leonhard, C., Wacker, K., Ringelstein, E.B., Okabe, M., Hickey, W.F., and Kiefer, R. (2003). Macrophage response to peripheral nerve injury: the quantitative contribution of resident and hematogenous macrophages. Lab. Invest. *83*, 175–185.

51. Muona, P., Jaakkola, S., Salonen, V., and Peltonen, J. (1993). Expression of glucose transporter 1 in adult and developing human peripheral nerve. Diabetologia *36*, 133–140. https://doi.org/10.1007/BF00400694.

52. Ornelas, S., Berthiaume, A.A., Bonney, S.K., Coelho-Santos, V., Underly, R.G., Kremer, A., Guérin, C.J., Lippens, S., and Shih, A.Y. (2021). Three-dimensional ultrastructure of the brain pericyte-endothelial interface. J. Cereb. Blood Flow Metab. *41*, 2185–2200. https://doi.org/10.1177/0271678X211012836.

53. Langen, U.H., Ayloo, S., and Gu, C. (2019). Development and cell biology of the blood-brain barrier. Annu. Rev. Cell Dev. Biol. *35*, 591–613. https://doi.org/10.1146/annurev-cellbio-100617-062608.

54. Reese, T.S., and Karnovsky, M.J. (1967). Fine structural localization of a blood-brain barrier to exogenous peroxidase. J. Cell Biol. *34*, 207–217.

55. Andreone, B.J., Chow, B.W., Tata, A., Lacoste, B., Ben-Zvi, A., Bullock, K., Deik, A.A., Ginty, D.D., Clish, C.B., and Gu, C. (2017). Blood-brain barrier permeability is regulated by lipid transport-dependent suppression of caveolae-mediated transcytosis. Neuron *94*. 581–594.e5. https://doi.org/10.1016/j.neuron.2017.03.043.

56. Siegenthaler, J.A., Sohet, F., and Daneman, R. (2013). 'Sealing off the CNS': cellular and molecular regulation of blood-brain barriergenesis. Curr. Opin. Neurobiol. *23*, 1057–1064. https://doi.org/10.1016/j.conb.2013.06.006.

57. Stan, R.V., Tse, D., Deharvengt, S.J., Smits, N.C., Xu, Y., Luciano, M.R., McGarry, C.L., Buitendijk, M., Nemani, K.V., Elgueta, R., et al. (2012). The diaphragms of fenestrated endothelia: gatekeepers of vascular permeability and blood composition. Dev. Cell *23*, 1203–1218. https://doi.org/10.1016/j.devcel.2012.11.003.

58. Shue, E.H., Carson-Walter, E.B., Liu, Y., Winans, B.N., Ali, Z.S., Chen, J., and Walter, K.A. (2008). Plasmalemmal vesicle associated protein-1 (PV-1) is a marker of blood-brain barrier disruption in rodent models. BMC Neurosci. *9*, 29. https://doi.org/10.1186/1471-2202-9-29.

59. Phoenix, T.N., Patmore, D.M., Boop, S., Boulos, N., Jacus, M.O., Patel, Y.T., Roussel, M.F., Finkelstein, D., Goumnerova, L., Perreault, S., et al. (2016). Medulloblastoma genotype dictates blood brain barrier phenotype. Cancer Cell *29*, 508–522. https://doi.org/10.1016/j.ccell.2016.03.002.

60. Bosma, E.K., van Noorden, C.J.F., Schlingemann, R.O., and Klaassen, I. (2018). The role of plasmalemma vesicle-associated protein in pathological breakdown of blood–brain and blood–retinal barriers: potential novel therapeutic target for cerebral edema and diabetic macular edema. Fluids Barriers CNS *15*, 24. https://doi.org/10.1186/s12987-018-0109-2.

61. Cattin, A.L., and Lloyd, A.C. (2016). The multicellular complexity of peripheral nerve regeneration. Curr. Opin. Neurobiol. *39*, 38–46. https://doi.org/10.1016/j.conb.2016.04.005.

62. Harrisingh, M.C., Perez-Nadales, E., Parkinson, D.B., Malcolm, D.S., Mudge, A.W., and Lloyd, A.C. (2004). The Ras/Raf/ERK signalling pathway drives Schwann cell dedifferentiation. EMBO J. *23*, 3061–3071. https://doi.org/10.1038/sj.emboj.7600309.

63. Sheu, J.Y., Kulhanek, D.J., and Eckenstein, F.P. (2000). Differential patterns of ERK and STAT3 phosphorylation after sciatic nerve transection in the rat. Exp. Neurol. *166*, 392–402. https://doi.org/10.1006/exnr.2000.7508.

64. Stierli, S., Imperatore, V., and Lloyd, A.C. (2019). Schwann cell plasticity-roles in tissue homeostasis, regeneration, and disease. Glia *67*, 2203–2215. https://doi.org/10.1002/glia.23643.

65. Elmore, M.R.P., Najafi, A.R., Koike, M.A., Dagher, N.N., Spangenberg, E.E., Rice, R.A., Kitazawa, M., Matusow, B., Nguyen, H., West, B.L., and Green, K.N. (2014). Colony-stimulating factor 1 receptor signaling is necessary for microglia viability, unmasking a microglia progenitor cell in the adult brain. Neuron *82*, 380–397. https://doi.org/10.1016/j.neuron.2014.02.040.

66. Lee, S., Shi, X.Q., Fan, A., West, B., and Zhang, J. (2018). Targeting macrophage and microglia activation with colony stimulating factor 1 receptor inhibitor is an effective strategy to treat injury-triggered neuropathic pain. Mol. Pain *14*. 1744806918764979. https://doi.org/10.1177/1744806918764979.

67. Weerasuriya, A., and Mizisin, A.P. (2011). The blood-nerve barrier: structure and functional significance. Methods Mol. Biol. *686*, 149–173. https://doi.org/10.1007/978-1-60761-938-3_6.

68. Roberts, T.C., Langer, R., and Wood, M.J.A. (2020). Advances in oligonucleotide drug delivery. Nat. Rev. Drug Discov. *19*, 673–694. https://doi.org/10.1038/s41573-020-0075-7.

69. Bennett, C.F., Kordasiewicz, H.B., and Cleveland, D.W. (2021). Antisense drugs make sense for neurological diseases. Annu. Rev. Pharmacol. Toxicol. *61*, 831–852. https://doi.org/10.1146/annurev-pharmtox-010919-023738.

70. Leavitt, B.R., and Tabrizi, S.J. (2020). Antisense oligonucleotides for neurodegeneration. Science *367*, 1428–1429. https://doi.org/10.1126/science.aba4624.

71. Dhuri, K., Bechtold, C., Quijano, E., Pham, H., Gupta, A., Vikram, A., and Bahal, R. (2020). Antisense oligonucleotides: an emerging area in drug discovery and development. J. Clin. Med. *9*, 2004. https://doi.org/10.3390/jcm9062004.

72. Finkel, R.S., Chiriboga, C.A., Vajsar, J., Day, J.W., Montes, J., De Vivo, D.C., Yamashita, M., Rigo, F., Hung, G., Schneider, E., et al. (2016). Treatment of infantile-onset spinal muscular atrophy with nusinersen: a phase 2, open-label, dose-escalation study. Lancet *388*, 3017–3026. https://doi.org/10.1016/S0140-6736(16)31408-8.

73. Zhao, H.T., Damle, S., Ikeda-Lee, K., Kuntz, S., Li, J., Mohan, A., Kim, A., Hung, G., Scheideler, M.A., Scherer, S.S., et al. (2018). PMP22 antisense oligonucleotides reverse Charcot-Marie-Tooth disease type 1A features in rodent models. J. Clin. Invest. *128*, 359–368. https://doi.org/10.1172/JCI96499.

74. Bonney, S.K., Coelho-Santos, V., Huang, S.F., Takeno, M., Kornfeld, J., Keller, A., and Shih, A.Y. (2022). Public volume electron microscopy data: an essential resource to study the brain microvasculature. Front. Cell Dev. Biol. *10*, 849469. https://doi.org/10.3389/fcell.2022.849469.

75. Liebner, S., Corada, M., Bangsow, T., Babbage, J., Taddei, A., Czupalla, C.J., Reis, M., Felici, A., Wolburg, H., Fruttiger, M., et al. (2008). Wnt/β-catenin signaling controls development of the blood–brain barrier. J. Cell Biol. *183*, 409–417. https://doi.org/10.1083/jcb.200806024.

76. Alvarez, J.I., Dodelet-Devillers, A., Kebir, H., Ifergan, I., Fabre, P.J., Terouz, S., Sabbagh, M., Wosik, K., Bourbonnière, L., Bernard, M., et al. (2011). The Hedgehog pathway promotes blood-brain barrier integrity and CNS immune quiescence. Science *334*, 1727–1731. https://doi.org/10.1126/science.1206936.

77. Alvarez, J.I., Katayama, T., and Prat, A. (2013). Glial influence on the blood brain barrier. Glia *61*, 1939–1958. https://doi.org/10.1002/glia.22575.

78. Lim, T.K.Y., Shi, X.Q., Martin, H.C., Huang, H., Luheshi, G., Rivest, S., and Zhang, J. (2014). Blood-nerve barrier dysfunction contributes to the generation of neuropathic pain and allows targeting of injured nerves for pain relief. Pain *155*, 954–967. https://doi.org/10.1016/j.pain.2014.01.026.

79. Serra, N.D., and Sundaram, M.V. (2021). Transcytosis in the development and morphogenesis of epithelial tissues. EMBO J. *40*, e106163. https://doi.org/10.15252/embj.2020106163.

80. Yang, B., Treweek, J.B., Kulkarni, R.P., Deverman, B.E., Chen, C.K., Lubeck, E., Shah, S., Cai, L., and Gradinaru, V. (2014). Single-cell phenotyping within transparent intact tissue through whole-body clearing. Cell *158*, 945–958. https://doi.org/10.1016/j.cell.2014.07.017.

81. Renier, N., Wu, Z., Simon, D.J., Yang, J., Ariel, P., and Tessier-Lavigne, M. (2014). iDISCO: a simple, rapid method to immunolabel large tissue samples for volume imaging. Cell *159*, 896–910. https://doi.org/10.1016/j.cell.2014.10.010.

82. Cattin, A.L., Burden, J.J., Van Emmenis, L., Mackenzie, F.E., Hoving, J.J.A., Garcia Calavia, N., Guo, Y., McLaughlin, M., Rosenberg, L.H.,

Quereda, V., et al. (2015). Macrophage-induced blood vessels guide Schwann cell-mediated regeneration of peripheral nerves. Cell *162*, 1127–1139. https://doi.org/10.1016/j.cell.2015.07.021.

83. Starborg, T., Kalson, N.S., Lu, Y., Mironov, A., Cootes, T.F., Holmes, D.F., and Kadler, K.E. (2013). Using transmission electron microscopy and 3View to determine collagen fibril size and three-dimensional organization. Nat. Protoc. *8*, 1433–1448. https://doi.org/10.1038/nprot.2013.086.
84. Schindelin, J., Arganda-Carreras, I., Frise, E., Kaynig, V., Longair, M., Pietzsch, T., Preibisch, S., Rueden, C., Saalfeld, S., Schmid, B., et al. (2012). Fiji: an open-source platform for biological-image analysis. Nat. Methods *9*, 676–682. https://doi.org/10.1038/nmeth.2019.

Please cite this article in press as: Malong et al., Characterization of the structure and control of the blood-nerve barrier identifies avenues for therapeutic delivery, Developmental Cell (2023), https://doi.org/10.1016/j.devcel.2023.01.002

STAR★METHODS

KEY RESOURCES TABLE

REAGENT or RESOURCE	SOURCE	IDENTIFIER
Antibodies		
Chicken polyclonal anti- 200kD neurofilament	Abcam	Cat# ab4680; RRID: AB_30456
Rat anti-mouse CD31 platelet endothelial cell adhesion molecule (PECAM) monoclonal	BD Biosciences	Cat# 550274; RRID: AB_393571
Rat F4/80 monoclonal (clone Cl:A3-1)	Bio-Rad	Cat#MCA497; RRID: AB_2098196
Rat Anti-Panendothelial Cell Antigen Monoclonal Antibody, Unconjugated, Clone MECA-32	BD Biosciences	Cat# 550563; RRID: AB_393754
Rabbit Glut1 polyclonal	Abcam	Cat# ab652; RRID: AB_305540
Rabbit Iba1 polyclonal	Wako	Cat# 019-19741; RRID: AB_839504
Rabbit Anti-CD34 Monoclonal Antibody Clone EP373Y	Abcam	Cat# ab81289; RRID: AB_1640331
Rabbit Anti-ZO-1 PAD Z-R1 Polyclonal	Invitrogen	Cat# 61-7300; RRID: AB_138452
Rabbit Anti-p75NTR (Neurotrophin Receptor) polyclonal	Millipore	Cat# 07-476; RRID: AB_310649
Rabbit Anti- PDGFRβ	Abcam	Cat# ab32570; RRID: AB_777165
Rabbit Anti-Caveolin1	Cell Signaling	Cat# 3267; RRID: AB_2275453
Rabbit Anti-CD146	Abcam	Cat# ab75769; RRID: AB_2143375
Goat Iba1 polyclonal	Abcam	Cat# ab5076; RRID: AB_2224402
Goat CD31/PECAM-1 Antibody	R & D Systems	Cat# AF3628; RRID: AB_2161028
Goat Anti-Mouse VE-cadherin Polyclonal	R & D Systems	Cat# AF1002; RRID: AB_2077789
Goat Anti-Mouse PDGF R alpha	R & D Systems	Cat# AF1062; RRID: AB_2236897
Mouse Anti-Reca1	Bio-Rad	Cat# MCA970R; RRID: AB_10015280
Mouse anti-Actin, α-Smooth Muscle - FITC monoclonal	Sigma-Aldrich	Cat# F3777; RRID: AB_476977
Mouse anti-Actin, α-Smooth Muscle – Cy3 monoclonal	Sigma-Aldrich	Cat#C6198; RRID: AB_476856
Mouse claudin-5 Monoclonal (4C3C2)	Thermo Fisher Scientific	Cat# 35-2500; RRID: AB_2533200
Mouse claudin-5 Monoclonal (4C3C2), Alexa Fluor 488	Thermo Fisher Scientific	Cat# 352588; RRID: AB_2532189
Mouse occludin (OC-3F10), Monoclonal, Alexa Fluor 488	Thermo Fisher Scientific	Cat# 331588; RRID: AB_2532185
Ulex europaeus agglutinin I (UEA I)	Vector Laboratories	Cat# FL-1061; RRID: AB_2336767
FluoroMyelin Red Fluorescent Myelin Stain	Invitrogen	Cat# F34652
Goat anti-Mouse Alexa Fluor 488	Thermo Fisher Scientific	Cat#A11001; RRID: AB_2534069
Goat anti-Mouse Alexa Fluor 647	Thermo Fisher Scientific	Cat#21235; RRID: AB_141693
Goat anti-Rat Alexa Fluor 488	Thermo Fisher Scientific	Cat#A11006; RRID: AB_2534074
Goat anti-Rabbit Alexa Fluor 594	Thermo Fisher Scientific	Cat#A11012; RRID: AB_2534079
Goat anti-Chicken Alexa Fluor 647	Thermo Fisher Scientific	Cat#A21449; RRID: AB_2535866
Donkey anti-Rat Alexa Fluor 488	Thermo Fisher Scientific	Cat#A21208; RRID: AB_2535794
Donkey anti-Rat Alexa Fluor 594	Thermo Fisher Scientific	Cat#A21209; RRID: AB_2535795
Donkey anti-Rat Alexa Fluor 647	Abcam	Cat#ab150155; RRID: AB_2813835

(*Continued on next page*)

Please cite this article in press as: Malong et al., Characterization of the structure and control of the blood-nerve barrier identifies avenues for therapeutic delivery, Developmental Cell (2023), https://doi.org/10.1016/j.devcel.2023.01.002

Continued

REAGENT or RESOURCE	SOURCE	IDENTIFIER
Donkey anti-Rabbit Alexa Fluor 488	Thermo Fisher Scientific	Cat#A21206; RRID: AB_2535792
Donkey anti-Rabbit Alexa Fluor 594	Thermo Fisher Scientific	Cat#A21207; RRID: AB_141637
Donkey anti-Rabbit Alexa Fluor 647	Thermo Fisher Scientific	Cat#A31573; RRID: AB_2536183
Donkey anti-Goat Alexa Fluor 405	Thermo Fisher Scientific	Cat#A48259; RRID: AB_2890272
Donkey anti-Goat Alexa Fluor 488	Thermo Fisher Scientific	Cat#A11055; RRID: AB_2534102
Donkey anti-Goat Alexa Fluor 594	Thermo Fisher Scientific	Cat#A11058; RRID: AB_2534105
Donkey anti-Goat Alexa Fluor 647	Thermo Fisher Scientific	Cat#A21447; RRID: AB_2535864
Biological samples		
Healthy adult nerve tissue	This paper	N/A
Chemicals, peptides and recombinant proteins		
Tamoxifen	Sigma-Aldrich	T5648
Griffonia (Bandeiraea) Simplicifolia Lectin I (GSL I, BSL I), Rhodamine	Vector Laboratories	RL-1102
Evans blue	Sigma-Aldrich	E2129
BSA	Sigma-Aldrich	A3294
Dextran 40KDa fluorescein lysine fixable	Thermo Fisher Scientific	D1845
HRP type II	Sigma-Aldrich	P8250
BSA-FITC	Invitrogen	A23015
Goat serum	Sigma-Aldrich	G9023
Donkey serum	Sigma-Aldrich	D9663
Formaldehyde 16%	TAAB Laboratories	F017
Formaldehyde (EM grade) 36%	TAAB Laboratories	F003
Glutaraldehyde (EM grade) 20%	TAAB Laboratories	G011
Osmium Tetroxide 2% aqueous	TAAB Laboratories	O005
Potassium Ferricyanide	Sigma-Aldrich	P-8131
AIN-76A Rodent Diet With 1,200 mg PLX5622 (Free Base)/kg	Research Diets, Inc. Plexxikon Inc	D11100404i
AIN-76A Rodent Diet	Research Diets, Inc. Plexxikon Inc	D10001i
Critical Commercial Assays		
PureLink RNA Micro kit	Thermo Fisher Scientific	Cat#12183016
SuperScript II	Thermo Fisher Scientific	18064014
MESA Blue qPCR Mastermix Plus Kit	Eurogentec	RT-SY2X-03+NRWOUB
Invitrogen Molecular Probes TSA Kit 25, with HRP-streptavidin and Alexa Fluor 594 tyramide	Thermo Fischer Scientific	Cat# T-20935
Experimental Models: Organisms/Strains		
Crl:CD(SD) Rattus norvegicus	Charles River Laboratories	001 Cat#734476; RRID:RGD734476
C57BL/6J	Charles River Laboratories	632 Cat# JAX_000664; RRID:IMSR_JAX:000664
P0-RafTR mouse	Napoli et al.[38]	Available from Jackson Stock# 018449
Oligonucleotides		
B2M forward: CAGTCTCAGTGGGGTGAAT reverse: ATGGGAAGCCGAACATACTG	This paper	N/A
Malat1 forward: TGGGTTAGAGAAGGCGTGTACTG reverse: TCAGCGGCAACTGGGAAA	This paper	N/A
Antisense Oligonucleotide Malat1: GCATTCTAATAGCAGC	IONIS Pharmaceuticals	N/A
Software and algorithms		
Fiji / ImageJ	Schindelin et al.[84]	https://imagej.net/Fiji/Downloads

(*Continued on next page*)

Continued

REAGENT or RESOURCE	SOURCE	IDENTIFIER
Prism	GraphPad	https://www.graphpad.com/ scientific-software/prism/
Imaris V9.1.2	Oxford Instruments	https://imaris.oxinst.com/
Plugin A posteriori shading correction	Developed by Maxime PINCHON, Laetitia PASQUET, Noël BONNET	https://imagej.nih.gov/ij/plugins/inserm514/
Adobe Photoshop CC	Adobe Systems	https://www.adobe.com/
Amira	ThermoFisher	https://www.thermofisher.com
iTEM	OSIS	https://www.olympus-sis.com/
Adobe Illustrator CC	Adobe Systems	https://www.adobe.com/
Other: Microscopes		
SPE3	Leica TCS SPE	405nm, 488nm, 561nm and 635nm
SPE8	Leica TCS SPE8 STED 3x	UV and white light laser 470–670nm
Multiphoton	Zeiss LSM880	405,488,561 and 633, lambda acquisition
LSM900	Zeiss LSM900	405, 488, 561 and 640 lasers
iSIM	Nikon GFP4 structure illumination microscope	Nikon Ti2 stand and Hamamatsu Flash 4 camera
Transmission electron microscope (TEM)	FEI Tecnai 12 Spirit BioTwin	OSIS morada
Serial Block Face SEM (SBF SEM)	Zeiss Sigma VP	Gatan 3View
Array tomography SEM (AT SEM)	Zeiss Gemini 300	Atlas 5, Sense Detector and tandem decel

RESOURCE AVAILABILITY

Lead contact

Further information and requests for resources and reagents should be directed to and will be fulfilled by the Lead Contact, Alison Lloyd (alison.lloyd@ucl.ac.uk).

Materials availability

This study did not generate new unique reagents.

Data and code availability

- Microscopy data reported in this paper will be shared by the lead contact upon request.
- This paper does not report original code.
- Any additional information required to reanalyse the data reported in this paper is available from the Lead Contact upon request.

EXPERIMENTAL MODELS AND SUBJECT DETAILS

Rodent husbandry

Mice and rats were group-housed in a 12-hour light/dark cycle (light between 07:00 and 19:00) in a temperature-controlled room (21.1 ± 1.1C) with free access to water and food at the Central Biological Service Unit at University College London, UK. Both male and female adult mice were used (6-12 weeks old). For experiments with the P0-RafTR strain, negative littermates were used as controls. Young male adult rats were used (6 -10 weeks old), weighing between 150 and 250g. All animal work was carried out in accordance to UK Home Office regulations.

Human tissue

Human nerves were obtained from the Royal National Orthopaedic Hospital in London, UK. Nerve sections were surgically removed from the wrists or legs of patients upon amputation for the treatment of osteosarcomas. Full ethical approval was in place and informed consent was obtained. Establishment UCL Cancer Institute. IRAS project ID: 27816. REC reference 20/YH/0088.

Please cite this article in press as: Malong et al., Characterization of the structure and control of the blood-nerve barrier identifies avenues for therapeutic delivery, Developmental Cell (2023), https://doi.org/10.1016/j.devcel.2023.01.002

METHOD DETAILS

Administration of substances

Tamoxifen (Sigma, T5648) was dissolved in ethanol at a concentration of 200mg/ml and further diluted in sunflower oil (Sigma, S5007) to reach a final concentration of 20mg/ml. The solution was vortexed for >3 hours to ensure total dissolution. Adult P0-RafTR and littermate controls were injected intraperitoneally or gavaged with a daily dose of tamoxifen at 150-200μg/g of body weight for 5 days and harvested on indicated days.

PLX5622 was formulated in AIN-76A chow at 1200ppm and was kindly provided by Plexxikon Inc. Animals were provided free access to either PLX5622-containing chow or control chow for 11-12 days before harvesting.

Intravenous tracers were injected into the tail vein of adult animals. Evans Blue solution was freshly prepared by dissolving Evans Blue (Sigma, E2129) and BSA (Sigma, A3294) in PBS to reach a concentration of 1% or 2% and 5%, respectively. Each animal was injected with 10μl/g of body weight and harvested 30 minutes later. HRP solution was prepared by dissolving 125mg of HRP type II (Sigma, P8250) in 2.5ml PBS. Each animal was injected with a single dose of 0.5mg/g of body weight and harvested at indicated time points. Lysine fixable BSA-FITC (Invitrogen, A23015) or 40kDa or 10kDa Dextran-FITC (Thermo Fisher Scientific, D1845) were prepared at 1.5 mg/ml in PBS. Animals were injected with 10μl/g of body weight and were harvested 30 minutes or 6 hours later. The contents of a 2mg vial of fluorescent lectin (Vector, RL-1102) were injected into 200g rats. Animals were harvested 5 minutes later.

Antisense oligonucleotides (ASO) were provided by Ionis Pharmaceuticals: Cy3-Malat1 #785313 stock solution at 24mg/ml, diluted in sterile PBS to inject mice at 1mg/ml solution at 10μl/g of body weight. Malat1 #556089 powder, reconstituted in sterile PBS, injected 10mg/ml at 10μl/g of body weight.

qRT-PCR

Immediately after dissection, sciatic nerves were snap-frozen in liquid nitrogen and stored at -80°C until further processing. Both sciatic nerves of each animal were crushed and homogenised on dry ice and then lysed in Trizol Reagent (Ambion). One volume of 70% ethanol was added, and this solution was loaded onto Purelink micro columns (ThermoFisher). RNA was extracted following the manufacturer's protocol, including the DNAse digestion step, with all centrifugations performed at ≥12,000g for 15 seconds. 500ng-1μg of RNA was then reverse-transcribed using Super-Script II Reverse Transcriptase (Invitrogen), following the manufacturer's instructions. Quantitative PCR (qPCR) was then performed using the MESA Blue qPCR Kit (Eurogentec). 0.5μl of template cDNA and 12.5μl of MESA blue qPCR MasterMix Plus kit (Eurogentec) including 0.8μl of forward and reverse primers mix (at 5μM) (see sequences in key resources table) were used per reaction in a 96-well plate. Water was used as a negative control. Relative expression values for each gene of interest were obtained after normalising to B2M. Primer sequence of genes of interest can be found in the key resources table.

Immunofluorescence

Sciatic nerves were dissected and fixed for a minimum of 4 hours in 4% paraformaldehyde (PFA)/PBS, cryoprotected in 30% sucrose/PBS overnight at 4°C, incubated in 50% OCT/30% sucrose/PBS for 2 hours, embedded in OCT and finally frozen in liquid nitrogen. Transverse (10μm) or longitudinal (10-30μm) cryosections were cut using a cryostat (Leica), permeabilised in 0.3% triton/PBS for 30 minutes, washed and then blocked in 10% goat or donkey serum (Sigma)/PBS for 1 hour at RT. Primary antibodies were diluted in 10% goat or donkey serum/PBS and incubated overnight at 4°C. Antibodies used were

Cav-1 (Cell Signaling 3267, 1:500), CD31 (BD Biosciences 550274, 1:100), CD31 (R & D Systems, AF3628, 1:200), CD34 (Abcam, ab81289, 1:400), CD146 (Abcam ab75769, 1:100), Claudin 5 (Thermo Fisher Scientific 35-2500, 1:500), F4/80 (Bio-Rad MCA497, 1:400), Glut1 (Abcam ab652, 1:500), Iba1 (Wako 019-19741, 1:500), Iba1 (Abcam ab5076, 1:500), Neurofilament (Abcam ab4680, 1:1000), $PDGF_R\beta$ (Abcam ab32570, 1:500), $PDGF_R\alpha$ (R&D Systems, AF1062, 1:100), p75NTR (Millipore, 07-476, 1:400), Reca1 (Bio-Rad MCA970R, 1:100), UEA I (Vector Laboratories FL-1061, 1:100). After washing with PBS, the appropriate fluorescent secondary antibodies Alexa Fluor 488, 594 or 647 (Thermo Fisher 1:400) and/or primary coupled antibodies αSMA-FITC (Sigma-Aldrich F3777, 1:1000), αSMA-FITC (Sigma-Aldrich C6198, 1:1000), Fluoromyelin (Life technologies F34652, 1:1000) were used with Hoechst for 1 hour at RT. Samples were mounted in Fluoromount G (Southern Biotechnology).

For samples requiring post-fixation, nerves were snap frozen and after cryosectioning, sections were immediately post-fixed with 4% PFA in PBS containing 0.084% Ca^{++} and 0.04% Mg^{++} (PBS++) for 10 min before the permeabilisation step. The protocol was followed as described above, except that PBS++ instead of PBS was used. Antibodies used were ZO-1 (Invitrogen 61-7300, 1:400), VE-cadherin (R & D Systems AF1002, 1:500), claudin-5 Alexa Fluor 488 (Thermo Fisher Scientific 352588, 1:100), occludin Alexa Fluor 488 (Thermo Fisher Scientific 331588, 1:100)) and PLVAP Clone MECA-32 (BD Biosciences, 550563, 1:100).

For claudin-5 primary antibody staining, the sections were blocked in 2% Fab fragment (Jackson Immunoresearch 715-007-003) /10% donkey serum/PBS overnight at 4°C instead of the blocking solution described above.

To reveal the presence of HRP in HRP-injected samples by light microscopy, an additional step was performed after the secondary antibody incubation. Samples were washed in PBS and incubated in an amplification buffer containing 0.1% tyramide reagent and 0.0015% H_2O_2 for 5 minutes in the dark at RT (Molecular Probes).

Human nerves were placed into 4% PFA/PBS upon dissection and kept at 4°C. The next day, smaller fragments were cut from the original piece and were placed in a fresh solution of PFA for 1-2 days. Following the fixation, nerves were cryopreserved and embedded in OCT following the same protocol as rodent nerves.

3D immunostaining

PACT protocol

To immunostain the junctional proteins of the perineurium and blood vessels, the PACT protocol was performed.[80] Briefly, nerves were fixed in 4% PFA overnight at 4°C. Nerves were then incubated for 24 hours in 4% acrylamide (40% acrylamide, BioRad), 0.25% 2,2'-Azobis (2-methylpropionamidine) dihydrochloride (Sigma-Aldrich) in PBS at 4°C. Nerves were degassed with nitrogen for 5 minutes and then left at 37°C for >6 hours, prior to being washed in PBS for one day at 37°C. All subsequent incubations took place at 37°C in a rotating device. Nerves were then incubated in 8% SDS for 4 days, with a fresh solution of SDS used on the third day. Nerves were washed in 0.01% sodium azide /PBS overnight, prior to the primary antibody incubation. Antibodies were diluted in 2% donkey serum/ 0.1% triton/ 0.01% sodium azide/PBS and incubated for 3 days, with fresh antibody added every day. The antibodies used were: VE-Cadherin (R&D systems AF1002, 1:10) and ZO1 (Invitrogen 61-7300, 1:10). Nerves were washed overnight in PBS and further incubated in the relevant secondary antibodies coupled to donkey Alexa Fluor fluorophores (1/100). Antibodies were diluted in 2% donkey serum/0.1% Triton/0.01% sodium azide/PBS and incubated for 4 days, with fresh antibody added daily for the first 3 days. Nerves were then washed in PBS O/N and incubated in Histodenz (Sigma D2158, 1.3 g/ml) overnight at 4°C, prior to being mounted in Histodenz using a mould (Grace bio-labs 664113) and dental glue (picodent twinsil).

iDisco protocol

Blood vessel and macrophage immunostaining of sciatic nerves were performed using the iDisco protocol.[81] Briefly, nerves were harvested and fixed in 4% PFA overnight at 4°C. The next day, nerves were left in PFA for 1 hour at RT, then washed in PBS and 0.2% Triton/PBS at RT for 1 hour each. Nerves were then incubated in 0.2% Triton /20% DMSO/PBS overnight at 37°C. The next day, the nerves were incubated in 0.1% Triton/0.1% Tween /0.1%(w/v) deoxycholate/0.1% NP40 /PBS O/N at 37°C. The samples were then washed in 0.2% Triton/PBS twice for 1 hour at RT, then incubated in 0.2% Triton /20% DMSO /0.3% glycine (w/v)/PBS O/N at 37°C. The samples were further washed in 0.2% Tween / 0.001% (w/v) heparin/PBS twice for 1 hour at RT, then blocked in 0.2% Triton /10% DMSO /6% donkey serum/PBS for 8 hours at 4°C. The nerves were then incubated in a blocking solution containing the primary antibodies (to Iba1, VE cadherin, and CD31, all 1:50) for 3 days at 37°C. Fresh antibody was added each day during this incubation. Nerves were then washed in 0.2% Tween /0.001% heparin (w/v)/PBS >8 hours and further incubated with a blocking solution containing the relevant secondary antibodies (1:100) for 3 days. Fresh antibody was added each day during this incubation. Nerves were then washed in 0.2% Tween /0.001% (w/v) heparin/PBS for 24 hours. Nerves were then cleared as follows: nerves were first dehydrated by a series of incubations in tetrahydrofuran (THF, Sigma) starting with 50% THF/50% water overnight, followed by 1 hour in 80% THF and twice for 1 hour in 100% THF. Nerves were then incubated in dichloromethane (DCM, Sigma) until the sample sank. Finally, nerves were incubated in DiBenzyl Ether (DBE, Sigma), and mounted in DBE using a mould (Grace-bio-labs 664113) and dental glue.

Transmission Electron Microscopy (TEM)

TEM was performed as described previously.[82] Briefly, nerves were fixed in a phosphate buffered solution (0.2M Na_2HPO_4: 0.2M NaH_2PO_4 in a 4:1 ratio) containing 2% glutaraldehyde and 2% PFA, for 1-7 days at 4°C. After 3 washes in phosphate buffer, the nerves were incubated in 2% Osmium Tetroxide for 2 hours at 4°C. The solution was rinsed off by 3 washes in water. The samples were then negatively stained in 2% Uranyl acetate for 45 mins at 4°C and washed in water. Nerves were then dehydrated by a series of incubations in increasing concentrations of ethanol: 5 mins in 25%, 5 mins in 50%, 5 mins in 70%, 10 mins in 90% and 4x10 mins in 100% ethanol. The dehydrated nerves were immersed in a propylene oxide solution for 3x10 mins, ensuring complete removal of residual ethanol in the tissue. Resin was prepared by mixing TAAB 812 (47%), DDSA (18.5%), MNA (32.5%) and DMP30 (2%). Nerves were then incubated for 1 hour in 50% resin-50% propylene oxide and a 100% resin overnight. The resin was refreshed in the morning. Nerves were embedded in resin in the evening and baked at 60°C overnight to allow the resin to polymerise. For HRP tracer experiments, fixed nerves were embedded in 2.8% low melting point agarose, and 150μm sections were prepared using a vibrating microtome (Leica). Sections were then washed in 0.05M Tris/HCl pH7.6 before undergoing DAB (3,3'-Diaminobezidine tetra-HCl) reaction as follows: 250μl of a 3% DAB solution (TAAB, D008) were added to 10ml of 0.05M Tris/HCl buffer and 7μl of 30% hydrogen peroxidase. Sections were incubated in this solution in the dark for 15 mins and further washed in the Tris buffer. After this, the sections were osmicated, stained, dehydrated and embedded as described above. Samples were trimmed and 70nm ultrathin sections were cut with a 45° diamond knife (DiatomeDiATOME) using an ultramicrotome (Leica UC7) and collected on 1x2 mm Formvar-coated slot grids. Images were acquired with a FEI Tecnai Spirit Bio-twin electron microscope (ThermoFisher) and a Morada G2 camera (Olympus Soft Imaging Solutions).

Serial Block Face SEM (SBF-SEM)

The samples were prepared essentially as described in Starborg et al.[83] Briefly, nerves were fixed in 0.2M phosphate buffer containing 2.5% PFA and 1.5% glutaraldehyde overnight at 4°C. Nerves were further incubated in 1% osmium tetroxide/1.5% potassium ferricyanide in water for 90 minutes at RT. After 3x 5minute washes in water, nerves were incubated in 1% tannic acid in 0.05M sodium cacodylate buffer for 2 hours at RT twice. Nerves were then washed in water again and treated in 1% osmium tetroxide for 30 minutes at RT. Nerves were then incubated in uranyl acetate (2%), dehydrated and embedded in epoxy resin as described above. Following this, 1-2mm thick cross sections were cut from the resin block, mounted with cyanoacrylate glue onto a specimen pin and 70nm thick sections were examined by TEM to identify the regions of interest. Samples on pins were then carbon-coated and mounted in an SEM equipped with a 3View microtome system (Gatan). The regions of interest on the block face were re-located in the SEM using backscattered electron detection and the imaging and cutting parameters were optimised for each sample. Data sets were collected

with section thickness between 120 and 150 microns in a Zeiss Sigma FEG-SEM coupled to Gatan 3View. Data was imported into Amira software (Thermo Fisher Scientific), where the cells of interest were manually segmented, reconstructed, and rendered in 3D.

Array Tomography SEM (AT-SEM)

Samples were prepared for scanning electron microscopy following a modified protocol (https://www.protocols.io/view/preparation-of-biological-tissues-for-serial.-block-36wgq7je5vk5/v2). Samples were washed in 0.1M sodium cacodylate buffer and post-fixed in 1% OsO4/1.5% potassium ferricyanide for 60 minutes at 4°C. Samples were then washed in distilled H2O and treated with 1% thiocarbohydrazide (TCH) for 20 minutes at RT, 2% osmium (OsO4) for 30 minutes at 4°C, 1% uranyl acetate (UA) overnight at 4°C, and lead aspartate for 30 minutes at 60°C, with intermediate washing in distilled H2O between each step. Dehydration and resin embedding was performed as previously described. Serial ultrathin sections were cut with a 45° diamond knife (DiatomeDiATOME) using an ultramicrotome (Leica UC7) and collected on ITO-coated coverslips. SEM imaging was performed using the SENSE backscatter detector on a Gemini 300 SEM (Zeiss) with an accelerating voltage of 4.5kV reduced to a landing energy of 1.5kV by application of a stage bias of 3kV, and at a working distance of 4mm. Serial imaging was performed using Atlas 5 software (Fibics), and images aligned using ImageJ.

Correlative light electron microscopy (CLEM)

CLEM was performed as described in Cattin et al.[82]. Briefly, nerves were fixed in 4% PFA overnight at 4°C. The next day, they were washed in ice-cold PBS for 30 mins, and embedded in 2.6% low melting point agarose. 100μm nerve transverse sections were then obtained using a vibratome. The sections were blocked in a solution of 10% goat serum/PBS for 30 mins, prior to being incubated in a solution of goat serum/PBS containing the primary antibodies against CD34 and F4/80 (1:400) for 1 hour. The sections were washed in PBS and further incubated for 1 hour in a solution of 10% goat serum/PBS containing secondary antibodies (1/400, Alexa fluor 594, 647 from Thermo Fisher Scientific), Hoechst (1:1000), or primary antibody against αSMA conjugated to FITC (1:500). All incubations were performed at 4°C. After this incubation, the sections were placed in a glass-bottomed petri dish and fixed with 2.6% low melting point agarose. Fluorescence images of regions of interest were acquired with a Leica SPE3 confocal microscope. Following acquisition, the sections were detached from the petri-dish and fixed for a second time in a 0.2M phosphate buffer containing 2.5% PFA and 1.5% glutaraldehyde for 30 mins at 4°C. The fixative was washed overnight in phosphate buffer at 4°C. The next day, the sections were subjected to the TEM protocol as described above. Ultra-thin sections were prepared with a microtome as described above, with particular care to collect the first sections, to be able to correlate with immunofluorescent images acquired earlier. TEM images were acquired and processed as described above. The correlation between the fluorescent images and the electron microscopy images were performed by hand, using FIJI, Adobe Photoshop and Adobe Illustrator.

Assessment of BNB function by Evans Blue

This experiment was performed as described in Napoli et al.[38] Briefly, nerves were snap-frozen in OCT upon dissection. Sections of 10μm were obtained using a cryostat (Leica) and mounted under a glass coverslip with fluoromount. The nerves were immediately imaged with a Zeiss Axio imager microscope using the 594 laser. Alternatively, sciatic nerves were dissected and fixed for a minimum of 4 hours in 4% paraformaldehyde (PFA)/PBS, cryoprotected in 30% sucrose/PBS overnight at 4°C, incubated in 50% OCT/30% sucrose/PBS for 2 hours, embedded in OCT and finally frozen in liquid nitrogen. Sections of 10μm were obtained using a cryostat (Leica) and mounted on a glass slide and immediately imaged with a Zeiss Axio imager microscope using the 594 nm laser.

Assessment of the permeability of the perineurium

The permeability of the perineurium was assessed *ex vivo*. Control nerves were harvested and immersed in a solution of 10% NaCl for 10 mins. NaCl-treated, control or P0-RafTR samples were then immersed in a solution containing 40kDa dextran-FITC (10 mg/ml) for 15 min for permeability evaluation (being careful not to immerse the extremities).

Light Microscope details

Confocal microscopes Zeiss LSM880 Multiphoton, Zeiss LSM900 and Leica TCS SP8 STED were used with 40x (1.3 NA) and 63x (1.4 NA) oil immersion objectives or 20x (0.8 NA) objective. Confocal microscope Leica SPE3 was used with 40x (1.15 NA) and 63x (1.3 NA) oil immersion objectives. Zeiss LSM880 Multiphoton was also used for multiphoton imaging and linear unmixing was performed after acquisition. Z step size ranged from 0.3-0.5μm. For super-resolution microscopy the Nikon GFP4 iSIM was used with 100x (1.45 NA) oil immersion objective with z-step size 0.1μm.

Experimental Design

The number of animals used for each experiment is stated in the relevant legend, with a minimum of 3 animal per experimental group. No data was excluded. Blinding was used when possible.

QUANTIFICATION AND STATISTICAL ANALYSIS

Image quantification

2D confocal images were opened and processed using Fiji,[84] Photoshop Software (Adobe) and Imaris. Parameters for optimisation of visualisation were applied to all images in an experiment. EM images were opened with Fiji and subjected to the "A posteriori shading correction" plugin developed by Maxime Pinchon, Laetitia Pasquet and Noël Bonnet and available online (automatic mode, 2x2). 3D Iba1 and CD31 immunostaining were deconvoluted using the Huygens software and opened using Imaris. The BSA-FITC images in Figure 5I were deconvoluted using Huygens software and opened using Fiji. Nikon iSIM images were deconvoluted using the 3D deconvolution module in the Nikon NIS-Elements software. Cell counting was performed using the built-in cell counter plugin in Fiji.

Endoneurial endothelial cell coverage

EndoEC coverage using 2D-TEM images was performed as follows: Using Fiji, the outer perimeter of each EC was manually drawn and measured. Cells participating in the coverage were identified as either embedded in the BM or in direct contact with it. The length of the cell/cell fragments embedded or in contact with the BM was measured and the total EC coverage was obtained with sum contacting cell/EC perimeter. Coverage of 3D-TEM was performed as follows: using Imaris, ECs and contacting cells were manually and individually drawn on each section in order to recreate the surface-rendering as visualised in the figures. The outer surface of the ECs was measured, as well as the surfaces of the contacting cells in direct contact with the ECs. A ratio of these values was calculated to obtain the cellular coverage of ECs. Pericyte coverage quantifications on 2D-TEM images were performed as follows: using Fiji, the outer perimeter of the EC was manually drawn and measured. Pericytes were identified by their localisation within the BM, and the length of the cell contact with the EC was measured. Pericyte coverage was obtained with sum pericyte/EC perimeter. Blood vessel lumen diameter was obtained using the following formula: π/ lumen perimeter. The lumen perimeter was measured by manually drawing it on 2D-TEM images using Fiji.

Cell:cell junction permeability

HRP penetration of cell:cell junctions was quantified using Fiji analysis of EM images. Penetration was determined by calculating the ratio between the length of the cell:cell junction, as visible on the 2D-TEM image, and the length of the black signal of the HRP/DAB reaction penetrating the length of the cell:cell junction. Using this method, a junction with a tight kissing point at the lumen side has a penetration ratio of 0 while a junction in which HRP can be observed throughout the whole length has a penetration ratio of 1.

Transcytosis levels

HRP transcytosis levels were calculated from 2D-TEM images using Fiji. The number of vesicles containing the black signal of the HRP/DAB reaction were counted manually. The area of cytoplasm was obtained using Fiji by measuring the total area of the blood vessel and subtracting the lumen area as well as the area of the nuclei of the ECs. Area of cytoplasm = total BV area – (area of lumen + area of EC nuclei).

Penetration of tracers into the endoneurium

Quantification of the penetration of tracers using fluorescent images were performed using Fiji. We first applied a fixed threshold to the tracers' signal (dextran-FITC, ASO-cy3, HRP). We then manually removed regions corresponding to the lumen of EndoBVs and the perineurium, as well as any surrounding tissue or empty/background area. To quantify EndoEC penetration, we measured the area of each EndoBV, subtracted the area of the lumen and calculated the tracer intensity within the EndoEC. To quantify penetration through the perineurium, we measured the area of the endoneurium and normalised the intensity to the analysed area.

Junctional protein expression was quantified using a Nikon iSIM. Whole 10μm longitudinal sections were scanned with the microscope using a 100x oil objective and expression of junctional proteins (claudin-5, occludin, VE-Cadherin, ZO-1) per BV (marked with CD31) counted.

Imaris 3D surface reconstruction and quantification

Images acquired from the Leica SP8 STED microscope were opened on Imaris (V9.1.2 and V9.9.1). Surfaces were created for each channel: For quantification of coverage, ECs (CD31), pericytes (αSMA), macrophages (F4/80) and or tactocytes (CD34). For quantification of Cav-1 expression, ECs (CD31), Caveolin-1 and nuclei (Hoechst). The same surface creation parameters were used for all images within an experiment, with minor adjustments in intensity threshold to compensate for dim staining. For quantification of coverage, a mask of the blood vessel surface was created in Imaris, exported to Fiji and filled using a macro, kindly provided by Tchern Lenn. The macro fills spherical objects through the whole z plane. This was imported into the Imaris file and used to create a surface for filled blood vessels. Internal controls were performed to confirm consistency by taking a ratio of the non-filled vs filled blood vessel. For the coverage of EndoBVs by pericytes, the "surface-surface coloc" function was applied to both surfaces. For the coverage of EndoBVs by macrophages and tactocytes, a distance transformation function was applied to the EndoBVs. This ensured that only pericytes in contact with EndoBVs were selected. Pericytes and EndoBVs were merged to quantify the coverage by macrophages or tactocytes using the "surface-surface coloc" function. "Surface-surface coloc" results in a new surface for the colocalisation area. The area of EndoBVs and "surface-surface coloc" was exported to Excel and quantified per EndoBV. For the quantification of Cav-1 expression, a surface was created for EndoECs (CD31) and masked onto the Cav-1 channel to remove all staining outside of the EndoECs. A surface for nuclei (Hoechst) was created and masked onto the Cav-1 channel to remove any staining not localised in the cytoplasm of the ECs. To quantify the expression of Cav-1, surfaces were created and the values for EndoEC volume and Cav1 within EndoEC volume were exported to Excel and Cav1/EndoEC volume quantified per EndoBVs.

Please cite this article in press as: Malong et al., Characterization of the structure and control of the blood-nerve barrier identifies avenues for therapeutic delivery, Developmental Cell (2023), https://doi.org/10.1016/j.devcel.2023.01.002

Statistical analysis

The number of animals used in each experiment is stated throughout the paper. For each quantification of fluorescence microscopy, a minimum of 5 images were quantified for each animal. Statistical analysis was carried out using Prism (Graphpad) statistical analysis software. All data are expressed as mean ± SEM unless otherwise indicated. Before applying statistical test, all datasets were subjected to a Shapiro-Wilk normality test to determine the choice of the test. Non-parametric tests were applied on non-normal data sets. When two experimental groups were compared, we used unpaired two-tailed Student's t test (parametric) or Mann-Whitney test (non- parametric) or Kolmogorov–Smirnov test (non-parametric to compare distributions). When more than 2 experimental groups were compared, we used a one-way analysis of variance (ANOVA), followed by Bonferonni's multiple comparisons test. P-values are indicated by asterisks as follows: *$p < 0.05$, **$p < 0.01$, ***$p < 0.001$, ****$p < 0.0001$.